Beam-ion confinement for different injection geometries

2009 Plasma Phys. Control. Fusion 51 125001

(http://iopscience.iop.org/0741-3335/51/12/125001)

Plasma Phys. Control. Fusion **51** (2009) 125001 (32pp) doi:10.1088/0741-3335/51/12/125001

Beam-ion confinement for different injection geometries

W W Heidbrink[1], M Murakami[2], J M Park[2], C C Petty[3], M A Van Zeeland[3], J H Yu[4] and G R McKee[5]

[1] University of California, Department of Physics and Astronomy, Irvine, CA 92697, USA
[2] Oak Ridge National Laboratory, PO Box 2008, Oak Ridge, TN 37831, USA
[3] General Atomics, PO Box 85608, San Diego, CA 92186-5608, USA
[4] University of California-San Diego, 9500 Gilman Drive, La Jolla, CA 92093, USA
[5] University of Wisconsin, Madison, WI 53726, USA

Received 6 May 2009, in final form 3 September 2009
Published 29 October 2009
Online at stacks.iop.org/PPCF/51/125001

Abstract

The DIII-D tokamak is equipped with neutral beam sources that inject in four different directions; in addition, the plasma can be moved up or down to compare off-axis with on-axis injection. Fast-ion data for eight different conditions have been obtained: co/counter, near-tangential/near-perpendicular and on-axis/off-axis. Neutron measurements during short beam pulses assess prompt and delayed losses under low-power conditions. As expected, co-injection has fewer losses than counter, tangential fewer than perpendicular and on-axis fewer than off-axis; the differences are greater at low current than at higher current. The helicity of the magnetic field has a weak effect on the overall confinement. Fast-ion D_α (FIDA) and neutron measurements diagnose the confinement at higher power. The basic trends are the same as in low-power plasmas but, even in plasmas without long wavelength Alfvén modes or other MHD, discrepancies with theory are observed, especially in higher temperature plasmas. At modest temperature, two-dimensional images of the FIDA light are in good agreement with the simulations for both on-axis and off-axis injection. Discrepancies with theory are more pronounced at low fast-ion energy and at high plasma temperature, suggesting that fast-ion transport by microturbulence is responsible for the anomalies.

(Some figures in this article are in colour only in the electronic version)

1. Introduction

Neutral beam injection (NBI) is a standard heating method in tokamak experiments. In many devices (including the DIII-D tokamak), it is the primary source of auxiliary heating. Verification of its proper operation is therefore essential. Beam ions are a major source of

energy, torque and particles, so a thorough understanding of beam behavior is crucial for plasma transport studies. The beam ions also can drive instabilities such as Alfvén eigenmodes [1, 2]. Understanding these instabilities requires accurate knowledge of the fast-ion distribution function. Finally, various current and future devices incorporate off-axis NBI for current profile control. If rapid fast-ion transport 'fills in' the hollow profile, the off-axis current will be insufficient to sustain a broad current profile.

The behavior of the fast ions produced by NBI has been the object of study for decades. Reviews of the topic [3, 4] state that, in the absence of MHD instabilities, nearly all reported measurements are consistent with classical theory. The initial deposition is described by multi-step ionization processes. Once ionized, the particles execute large orbits that depend on constants of motion such as the energy E, the magnetic moment μ and the canonical toroidal angular momentum P_ϕ; many of the predicted orbits have been observed experimentally. On a longer timescale, the fast ions decelerate and pitch-angle scatter as predicted by Coulomb scattering theory. For energetic ions, the observed spatial transport is consistent with the low levels of diffusion predicted by neoclassical theory. Measured neutron rates agree with predictions based on these theories. In the last decade, many new techniques and devices have reconfirmed this basic picture [5–21].

Despite this substantial body of research, new studies are warranted. The conventional explanation for the low transport of fast ions is that, owing to their large gyroradii and drift orbits, energetic ions phase average over the fluctuations that cause thermal particle transport [22–24]. The averaging in space is analogous to the temporal phase-averaging that underlies gyrokinetic theory. Transport is reduced by factors such as $J_0(\rho_f/\Delta_r)$, where J_0 is the Bessel function, ρ_f is the fast-ion gyroradius and Δ_r is a characteristic spatial scale of the microturbulence. Assuming that Δ_r scales with thermal-particle orbit size, theory predicts that fast-ion transport decreases when the ratio of fast-ion energy to thermal-temperature E/T increases. Nearly all of the transport measurements with effective diffusion $\lesssim 0.1\ \mathrm{m^2\ s^{-1}}$ cited in [3] are for large values of E/T (typically $\gg 10$). Recent studies of neutral beam current drive (NBCD) on ASDEX Upgrade suggest that larger fast-ion diffusion may occur when the injection energy is closer to the plasma temperature [25]. Discrepancies with theory may also occur during off-axis injection into JT-60U [26]. During on-axis injection of tritium beams in JET, anomalous neutron signals are sometimes observed [27]. Thus, one reason to re-examine this topic is to make accurate measurements of fast-ion confinement in the moderate energy regime ($E/T \lesssim 10$).

A second reason to revisit beam-ion confinement is that the applicability of the phase-averaging theory sketched above is controversial. Some authors [28, 29] stress that, for small values of Kubo number (ratio of decorrelation time to fast-ion time of flight), phase-averaging does not occur. For situations where phase-averaging is applicable, different scalings with E/T are predicted. Reference [30] predicts that, in the high-energy limit, the diffusivity of passing fast ions D_B is proportional to $(E/T)^{-3/2}$, while [31] predicts $(E/T)^{-1}$ scaling for electrostatic turbulence and no reduction for electromagnetic microturbulence. Both gyromotion and drift motion are important but phase-averaging could be valid for the gyromotion without applying for the drift motion [32, 33]. One paper suggests significant transport of alphas by microturbulence in ITER [34], while another insists that the conventional expectation of small transport is correct [35].

A third reason to revisit this topic is that a new diagnostic method has become available, the fast-ion D-alpha (FIDA) technique [13]. FIDA provides local fast-ion measurements with intrinsic spatial resolution of a few centimeters in a transverse dimension; it also provides some energy resolution [36]. In initial experiments in low-temperature MHD-quiescent plasmas, FIDA profiles and spectra are in good agreement with classical predictions [17].

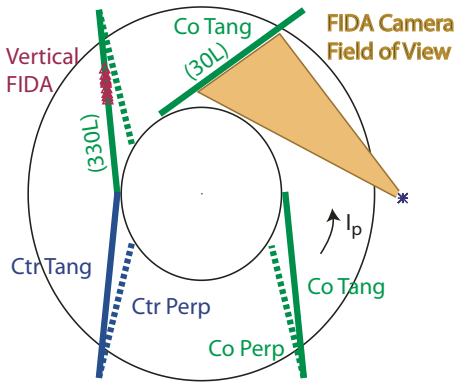

Figure 1. Plan view of the DIII-D tokamak showing the centerlines of the four near-tangential (solid) and three near-perpendicular (dashed) neutral beam injectors employed in this study. The radial location of the FIDA fiber views and the field of view for two dimensional FIDA imaging are also shown. The 330L source is the imaging beam for vertical FIDA and the 30L source is the imaging beam for two-dimensional FIDA imaging.

This paper presents a careful quantitative study of beam-ion confinement based on neutron and FIDA data. A companion paper [37] reports measurements of NBCD in many of the same discharges. The measurements are compared with predictions based on the NUBEAM module in the TRANSP code [38]. NUBEAM uses Monte Carlo methods to compute the classically expected distribution function; it also can include *ad hoc* spatial diffusion in its calculation. Our study relies heavily on relative comparisons of different injection geometries in the same discharge, which reduces the sensitivity of the TRANSP predictions to uncertainties in plasma parameters. DIII-D has one beam line that is a mirror image of the others, allowing convenient comparison of injection along or against the plasma current (called 'co' and 'counter' injection). The plasmas can also be readily shifted vertically to compare on-axis with off-axis injection. In discharges with very dilute fast-ion populations, the data agree with classical theory, with an upper bound on the effective diffusion of $<0.5\,\mathrm{m^2\,s^{-1}}$. At higher beam power, some discharges are consistent with the classical NUBEAM predictions but, in other cases, discrepancies larger than the estimated errors are observed. The radial, energy and temperature dependences of these discrepancies suggest that transport by microturbulence distorts the fast-ion distribution function [39].

The paper begins with a discussion of the beam geometry, discharge conditions and diagnostics (section 2). Next, neutron measurements during short beam 'blips' are presented (section 3). Section 4 is on FIDA and neutron measurements in discharges with at least 3 MW of injected power. Section 5 shows that fast-ion transport by microturbulence can account for the discrepancies. Section 6 contains the conclusions.

2. Apparatus

The data in this paper are from a set of NBCD experiments conducted on five different days in 2008. The seven DIII-D neutral beam sources inject full-energy deuterium neutrals at 74–81 keV. The beams all inject in the horizontal midplane. The tangency radius of the sources is either $R_{\mathrm{tan}} = 74\,\mathrm{cm}$ or 115 cm (figure 1); some sources inject in the direction of the plasma current and others inject in the counter-current direction. The plasma major radius R is about 170 cm. The plasma current is always in the counter-clockwise direction for these

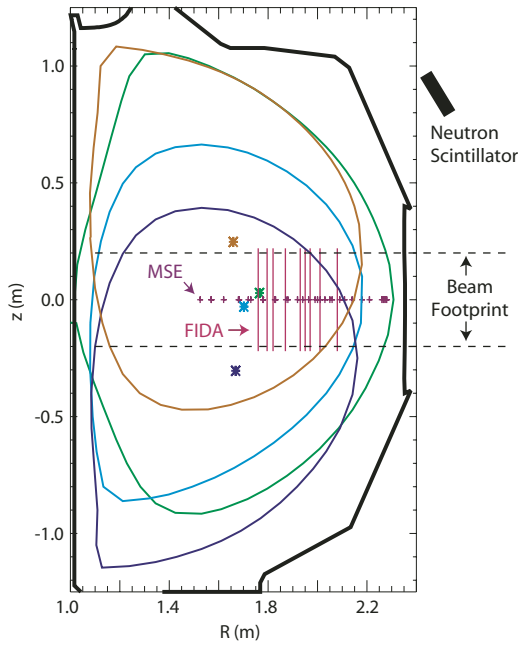

Figure 2. Elevation of the DIII-D vessel, together with the last closed flux surface (line) and magnetic axis (*) for four representative shapes. The radial locations of MSE (+) [40] and vertical FIDA channels (|) are also shown. The approximate height of the injected neutral beams are indicated by the dashed lines. The location of the neutron scintillator is also shown.

experiments but the toroidal field is either in the counter-clockwise direction (called $+B_T$) or in the clockwise direction (called $-B_T$). The toroidal field is approximately $|B_T| = 2.0$ T for all of the discharges in this study. At the magnetic axis, the vertical extent of the injected neutrals is $\sim\pm 20$ cm. Typical current fractions as the beam enters the plasma are 55% in the full-energy component, 29% in the half-energy component and 16% in the third-energy component.

Many of the plasmas have smaller cross section than usual (figure 2). The magnetic axis of the small plasmas are shifted upward or downward $z_0 \simeq \pm 30$ cm to inject the beams off-axis. Later in the discharge, the magnetic axis is centered ($z_0 \simeq 0$) to study on-axis injection.

The calculated orbits are quite different for the different injection geometries. Figure 3 shows full-energy orbits of neutrals that ionize at the same (R, z) position for the four different injection angles and for on-axis and off-axis injection. The co-current orbits are better confined than the counter-current orbits because, as is well known [41], trapped particles are born on the outer leg of their banana orbit during co-current injection, while counter-current orbits are born on the inner leg of their banana. It is also evident in the figure that the more perpendicular ($R_{tan} = 74$ cm) geometry produces orbits that are more deeply trapped than the more tangential ($R_{tan} = 115$ cm) geometry. Comparison of off-axis orbits (top row) with on-axis orbits (bottom row) shows that the confinement is significantly better for on-axis injection for all injection angles.

Figure 4 shows fast-ion distribution functions computed by NUBEAM for one of the discharges in this study. Contour plots with higher beam density correspond to better confinement. The differences observed for the representative orbits of figure 3 are preserved when the entire distribution is considered. For all angles of injection, the confinement is better for on-axis injection than for off-axis injection. Co-injection is better than counter. For both

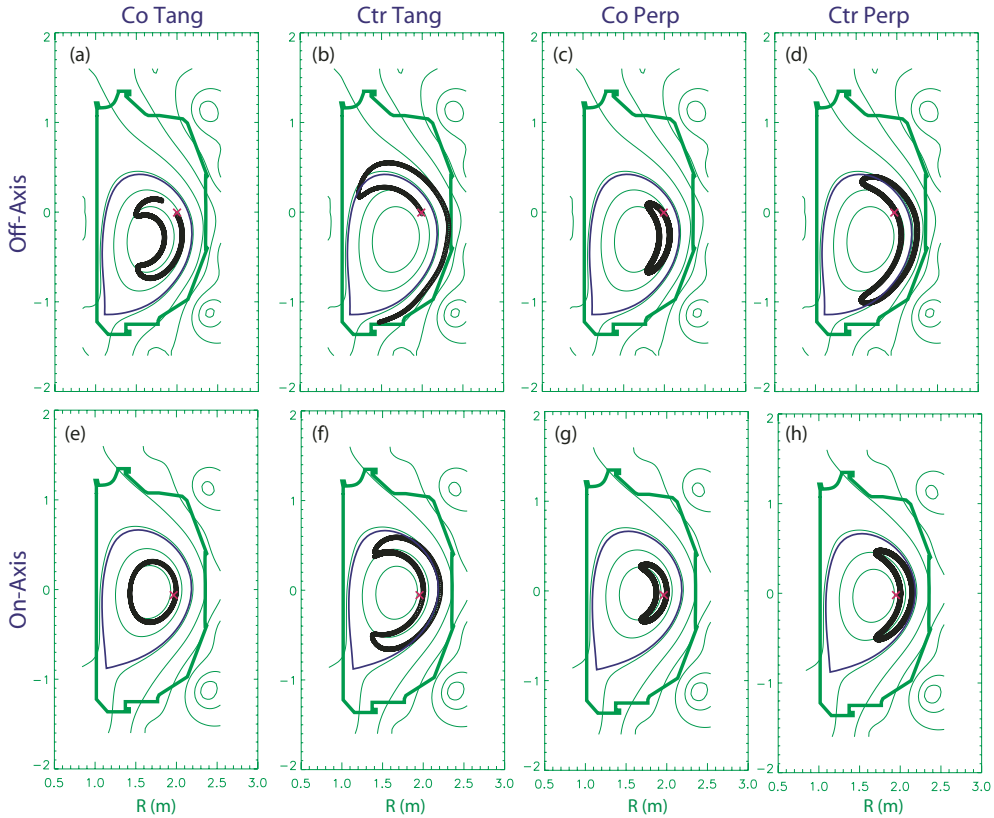

Figure 3. Projections of representative orbits in a down-shifted small plasma with $-B_T$ (top row) and in the same small plasma after it was centered (bottom row) for co-tangential (*a*), (*e*), counter-tangential (*b*), (*f*), co-perpendicular (*c*), (*g*) and counter-perpendicular (*d*), (*h*) angles of beam injection. All eight orbits are launched at the same (R, z) location with 80 keV of energy with the velocity vector of the beam centerline. $I_p = 0.9$ MA.

co- and counter-injection, a more tangential injection angle yields better confinement. Another feature evident in figure 4 is that the centroid of the population occurs at larger minor radius for off-axis than for on-axis injection, as expected. The dependence on pitch ($\chi = v_\parallel/v$ defined relative to the plasma-current direction) also contains interesting information. In a contour plot of this sort, passing particles from a tangentially injected source are asymmetric in pitch, while trapped particles form a vertical column centered around $\chi = 0$. The counter beams produce more trapped particles than co beams and the perpendicular beams produce more trapped particles than tangential beams.

For off-axis injection, the fast-ion population depends on the helicity of the field line [42]. For injection with a negligible poloidal field, the initial pitch of the velocity vector relative to the field is $\chi_0 \simeq v_\phi/v = R_{tan}/R$. For off-axis injection with appreciable poloidal field, one field-line helicity shifts χ to larger values, while the other helicity shifts χ to smaller values. For the helicity that increases χ, the number of passing particles increases and the orbit shifts decrease, so most of the particles remain close to the flux surface of their birth. Because this helicity has a well-localized fast-ion population with large values of $v_\parallel$, it is favorable for off-axis NBCD. On the other hand, the opposite helicity has lower values of χ, more trapped

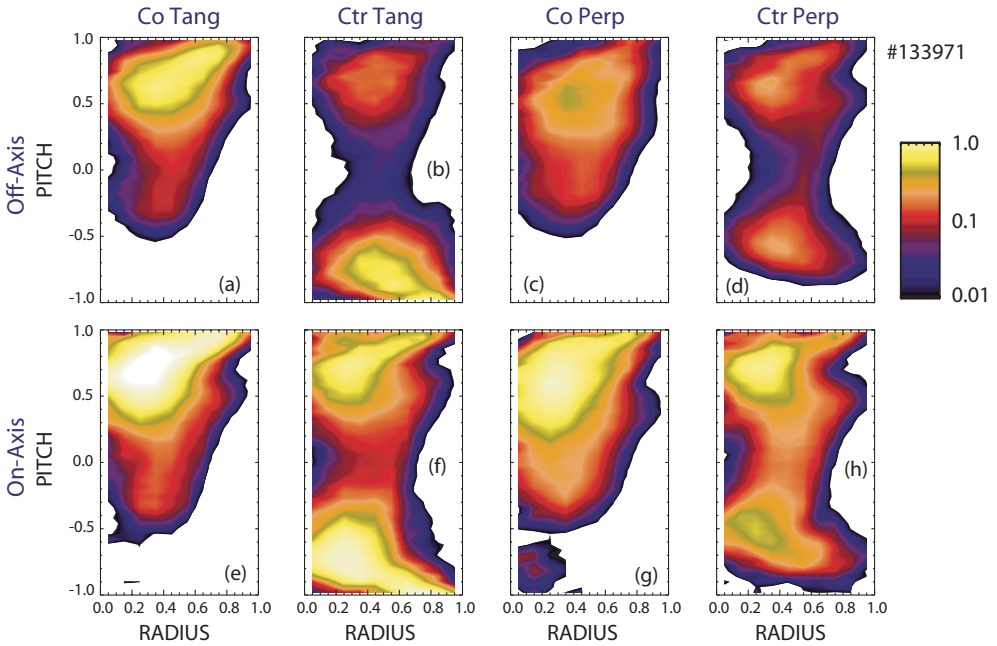

Figure 4. TRANSP beam-ion distribution functions after 75 ms of beam injection by the various types of beams for injection into a small downshifted plasma with $+B_T$ (top row) and for injection into the same small plasma after it was centered later in the discharge (bottom row). The abscissa is the normalized minor radius, the ordinate is the pitch χ and the distributions are averaged over energies between 60 and 83 keV. The same logarithmic intensity scale is used in all eight panels. $I_p = 0.9$ MA.

particles and more orbits that approach the magnetic axis. This helicity is less favorable for NBCD. Figure 5 shows the calculated distribution functions in a pair of matched discharges with opposite helicities. With the favorable helicity for current drive (figure 5(*a*)), the center of the distribution is at larger minor radius and larger pitch than for the unfavorable NBCD helicity (figure 5(*b*)). The unfavorable helicity has more trapped ions.

Neutron detectors and FIDA instruments are the primary diagnostics for this study. The neutron detectors consist of a plastic scintillator, a ZnS scintillator and fission and BF_3 counters [43]. For reasons that are not fully understood, the uncertainty in the absolute calibration for the fission counters was greater than the usual 15% during the 2008 campaign. An additional uncertainty in the absolute calibration is associated with the large vertical shifts of the plasma. The neutron scintillators are close to the plasma (figure 2) but, based on formulas in [44], the collection efficiency of the plastic scintillator changes only a few per cent due to the vertical shifts. The counters are several meters from the vacuum vessel, so the expected impact of the shifts on their collection efficiencies is even smaller. The temporal evolution of both scintillator signals are consistent with the neutron counter data but, because the scintillators have superior temporal resolution, this paper relies primarily on relative neutron measurements by the scintillators during a particular phase of the discharge.

The FIDA measurements are from three instruments. The best time resolution is from a spectrometer that measures the full spectrum for two radial positions with a vertical view [36]. Absolutely calibrated data are available for measurements of the blue-shifted spectrum for seven radial fibers that also have vertical views (figures 1 and 2). The spatial resolution of

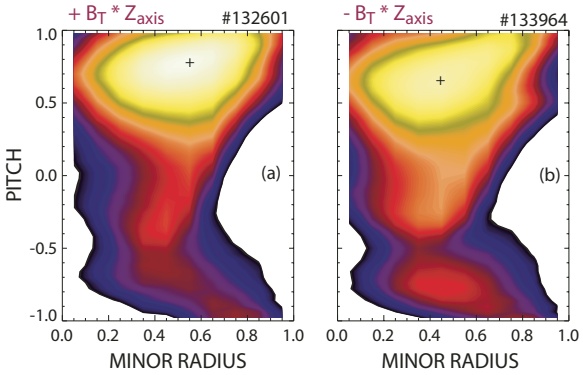

Figure 5. TRANSP beam-ion distribution functions in two nearly identical down-shifted plasmas during co-tangential injection with either (*a*) $-B_T$ or (*b*) $+B_T$. The axes are the same as in figure 4. The + symbols mark the peak of the distribution. $I_p = 0.9$ MA.

both instruments is determined by the beam footprint in the vertical direction and (primarily) by the intrinsic spatial resolution of the FIDA technique (∼3 cm) in the radial direction. The light collection efficiency of the calibrated system decreased ∼30% during the 2008 campaign; in this paper, the intensity calibration from immediately after the campaign is employed. The third FIDA instrument uses a tangentially viewing camera in conjunction with a bandpass filter to obtain two-dimensional measurements of the FIDA light [45]. Owing to the measurement geometry (figure 1) and filter properties, the measured signal is produced primarily by counter-circulating fast ions. All of the FIDA data are derived by subtracting the light when the modulated imaging beam is off from the light when the beam is on; uncertainty in the background subtraction is the dominant source of error [36]. To compare with theory, the distribution function predicted by TRANSP is input into a FIDA simulation code [13] that predicts the spectral radiance.

The beam modulation patterns (figure 6) are optimized to obtain high quality neutron and FIDA data. To diagnose the behavior of dilute fast-ion populations, short beam 'blips' are injected into steady-state ohmic plasmas (figure 6(*a*)). Typically, one beam is on for 6 ms, all beams are off for 44 ms, then a different beam is injected. For optimal vertical FIDA data, each type of beam injects for 80 ms (a time longer than the typical slowing-down time), while the vertical FIDA imaging beam steadily injects at 50% duty cycle (figure 6(*b*)). For two-dimensional FIDA imaging, the 30L imaging beam viewed by the camera alternates with a counter beam that produces a counter-circulating fast-ion population (figure 6(*c*)). Finally, for NBCD measurements, co-tangential beams inject steadily at various power levels (figure 6(*d*)); meanwhile, the 330L co-tangential beam viewed by the vertical FIDA system is modulated, and a counter-tangential beam used by the motional Stark effect (MSE) diagnostic is on for short diagnostic blips.

The discharge conditions are usually very steady. Figure 7 shows an example from one of the NBCD discharges. The steady conditions facilitate extensive averaging of the FIDA data to reduce statistical error. The steady-state portion persists for many current diffusion times, so the q profiles are relaxed and most of the discharges with cyclic patterns of beam injection (figures 6(*a*)–(*c*)) have sawteeth. In contrast, discharges with steady off-axis co-tangential injection (figure 6(*d*)) generally do not have sawteeth.

Typical plasma parameters for an off-axis case with average injected beam power of $P_B = 3.9$ MW are shown in figure 8. Particularly during off-axis injection, some important

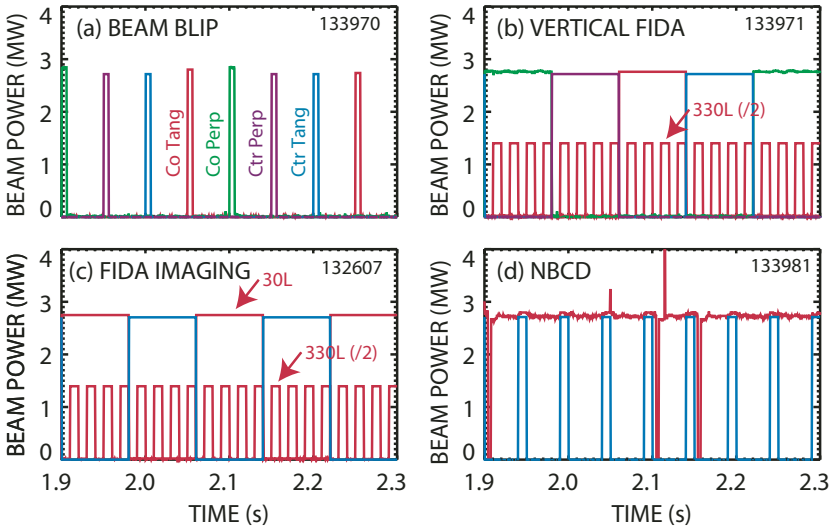

Figure 6. The four types of beam injection patterns employed in this study. (*a*) Repetitive cycles of beam blips for the four angles of beam injection. (*b*) Repetitive cycles of injection for 80 ms for the four angles of beam injection. The 330L beam used for vertical FIDA measurements (with its power divided by two for clarity) injects at 50% duty cycle throughout. (*c*) For two-dimensional FIDA imaging, the 30L beam that neutralizes the fast ions alternates with the counter-tangential beam. The 330L beam is modulated at 50% duty cycle for vertical FIDA measurements. (*d*) For NBCD, the 330L beam is modulated for vertical FIDA measurements and other co-tangential sources supply additional power to produce plasmas with variable amounts of co-tangential power.

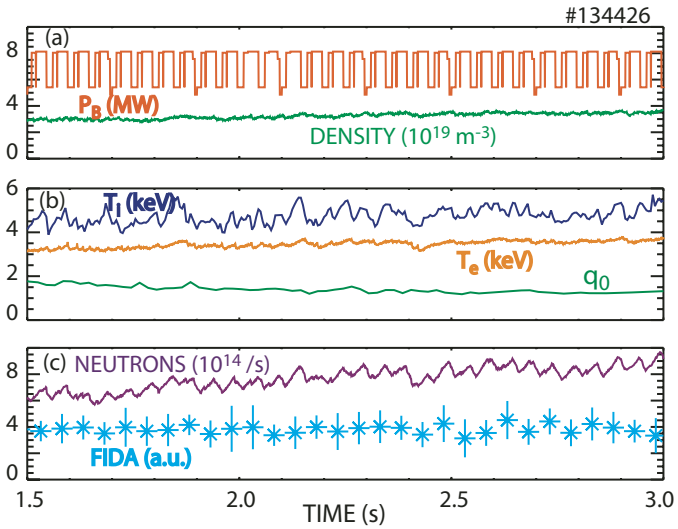

Figure 7. Time evolution of (*a*) the injected beam power P_B and line-average electron density, (*b*) T_i and T_e at $\rho \simeq 0.32$ and central safety factor q_0 and (*c*) neutron rate and FIDA radiance at $\rho \simeq 0.35$. $I_p = 0.9$ MA.

parameters have larger uncertainties than normal. The solid lines in the figure are the most likely profiles in this particular discharge, while the dashed lines represent variations near the limits of plausibility that are used in the sensitivity study described below. The baseline neutral density profile (figure 8(*a*)) is derived from cold D-alpha measurements [46]. The electron

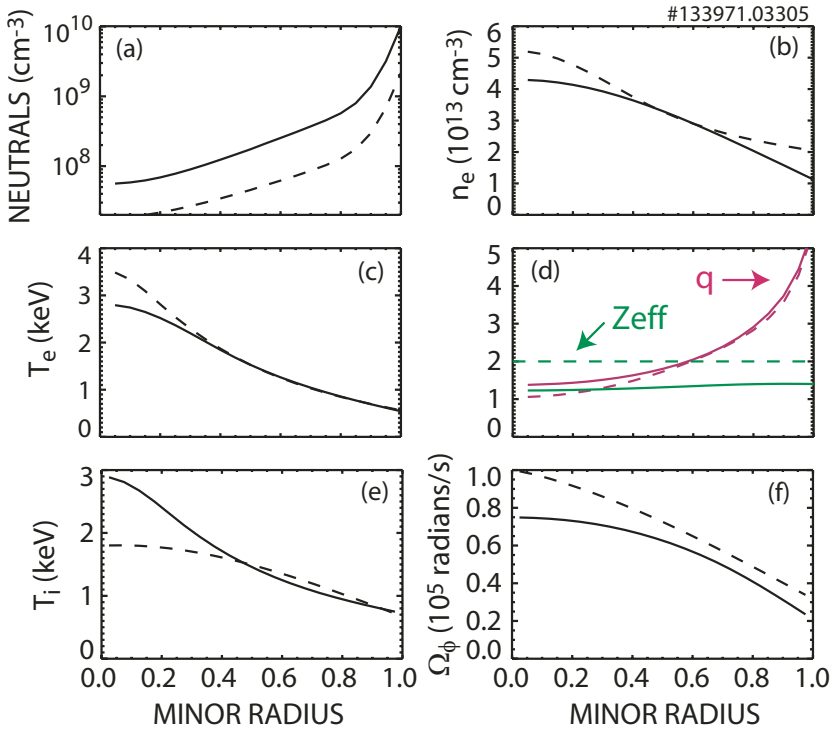

Figure 8. Profiles of (*a*) neutral density, (*b*) electron density, (*c*) electron temperature, (*d*) $Z_{\rm eff}$ and q, (*e*) ion temperature and (*f*) toroidal angular frequency for a down-shifted discharge with $+B_{\rm T}$ and $I_{\rm p} = 0.9$ MA. The abscissa is the normalized square root of the toroidal flux. The solid lines are the best-fit profiles used for the baseline case in the TRANSP sensitivity studies, while the dashed lines are extreme variations near the limits of plausibility.

density and temperature profiles (figures 8(*b*) and (*c*)) are quite uncertain near the magnetic axis for off-axis injection because neither the Thomson scattering [47] nor the electron cyclotron emission (ECE) diagnostic [48] view the plasma core in these shifted plasmas. This is also the case for the ion temperature (figure 8(*e*)) and toroidal rotation (figure 8(*f*)) profiles derived from charge-exchange recombination (CER) spectroscopy [49]. The carbon impurity density from CER implies a quite low value of $Z_{\rm eff}$ in these discharges (figure 8(*d*)); other impurities may make $Z_{\rm eff}$ higher. Because there are no MSE channels at the magnetic axis for off-axis injection (figure 2), the central value of q is quite uncertain (figure 8(*d*)), although the presence or absence of sawteeth may put constraints on q_0.

MHD instabilities such as tearing modes or Alfvén eigenmodes can cause fast-ion transport [3] but are not the focus of this study. Magnetic [50], ECE [51] and CO_2 interferometer [52] diagnostics detect low-frequency MHD and fast-ion driven instabilities that could affect the fast-ion confinement. Except where noted explicitly, the discharges discussed here have negligible levels of these modes.

3. Beam blip data

To study the confinement of dilute populations of fast ions, short beam pulses are injected (figure 6(*a*)). The neutron rate rises approximately linearly during the short pulses, then

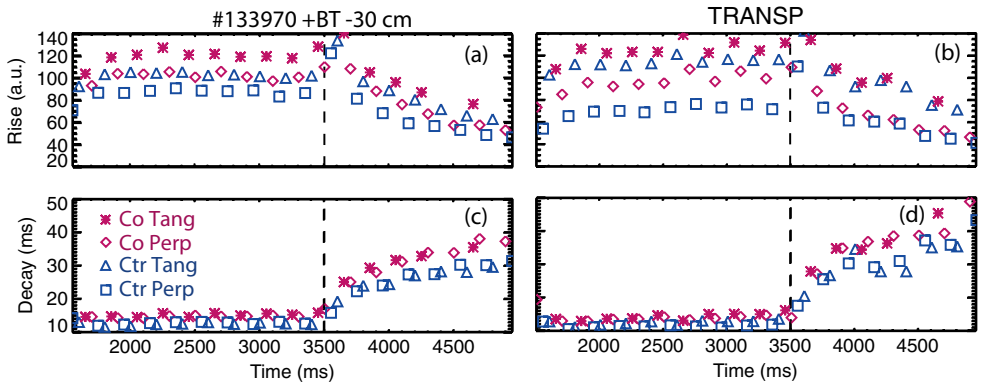

Figure 9. Experimental and theoretical rates of rise (*a*), (*b*) and decay times (*c*), (*d*) for a small plasma with $+B_T$. The magnetic axis is at $z_0 = -30$ cm until 3500 ms and reaches the midplane ∼70 ms later. The angle of beam injection is represented by the symbols.

decays approximately exponentially, as in figure 3 of [12]. The rate of rise of the neutron rate $\dot{S}_n$ is approximately [12]

$$\dot{S}_n = \dot{N}_b n_d \langle \sigma v \rangle, \tag{1}$$

where $\dot{N}_b$ is the rate of increase in the beam-ion population, n_d is the deuterium density and $\langle \sigma v \rangle$ is the d–d fusion reactivity. The signal decays following the beam pulse because the fast ions decelerate. The decay rate ν_n is faster than the energy deceleration rate ν_E because the fusion reactivity decreases rapidly with energy, $\nu_n \simeq 2.6\nu_E$. The two phases of the neutron signal have a simple physical interpretation. The rise of the neutron signal is a measure of the prompt confinement of the injected beam ions on their first 100–1000 drift orbits. If the signal decays faster than predicted by classical Coulomb scattering theory, it is an indication of enhanced fast-ion losses on the collisional timescale.

The observed neutron signals are fit extremely well by the simple model equations given in [12] for virtually all of the beam blips in this study. (Examples of typical raw data appear in figure 12.) Specifically, the neutron rate increases as $\dot{S}_n = c - \nu_n S_n$ during the beam pulse and decreases as $\dot{S}_n = -\nu_n S_n$ after the pulse. (Here c and ν_n are fitted constants.) The fits to this simple model are excellent, with nearly all fits having a reduced chi-squared less than unity. To compare confinement for different beam injectors with slightly different injection energies and currents I_B, the fitted constant c during the rise phase is divided by $\langle \sigma v \rangle$ (evaluated at the injection energy) and by I_B. Thus, the rise constant is a direct measure of prompt confinement. The decay fits are typically applied until the signal has decayed to $1/e$ of its peak value, so the decay data provide information on the delayed losses of fast ions with energies $\gtrsim$50 keV.

An example of the fitted rise constants and $1/\nu_n$ decay times for a representative discharge are shown in figure 9. In this discharge, the plasma was shifted downward to $z_0 \simeq 31$ cm in the first half of the discharge, then shifted back to the midplane from 3500 to 3600 ms. The electron density was larger in the off-axis injection phase than in the on-axis injection phase, so the rise constant is larger but the decay time is shorter early in the discharge. (The rise is proportional to the thermal deuterium density n_d but the decay time is inversely proportional to n_e because the slowing-down time is inversely proportional to the density.) Similarly, the gradual decrease in the rise constant and increase in decay time during the on-axis phase is due to a gradual decrease in n_e. Generally, however, the plasma conditions are rather steady, so

these data are useful for comparison of the confinement of the different angles of beam injection. The rise constant is largest for co-tangential injection, indicating that these beam ions are the best confined. Conversely, as expected, the rise constant is smallest for the poorly confined orbits deposited by near-perpendicular counter-injection. When the injection is off-axis, the co-perpendicular confinement nearly equals the counter-tangential confinement but, in the on-axis phase, the counter-tangential confinement is slightly better than the co-perpendicular confinement. During the decay phase, the co-injected ions are better confined for both on- and off-axis injection.

To compare with theory, the time-evolving plasma parameters are entered into the TRANSP code and the neutron rate is calculated. The TRANSP neutron prediction is fitted in the same manner as the experimental data. Once again, the fits to the simple rise and fall model equations are excellent. As shown in figure 9, the theoretical predictions have much in common with the experimental measurements but some differences are apparent. In agreement with the experiment, the modeling predicts the best prompt confinement for co-tangential injection and the worst prompt confinement for counter-perpendicular injection. Theory also correctly predicts longer decay times for co-injection than for counter-injection. However, the prompt confinement of counter-tangential ions is overestimated relative to co-perpendicular ions.

In both theory and experiment, the confinement is better for on-axis injection than for off-axis injection. For experiment, equation (1) implies that confined beam ions are injected during the beam pulse at the rate $\dot{N}_b \propto \dot{S}_n/n_e$. For a discharge where the density was nearly constant at the transition from off-axis to on-axis injection, the neutron data imply that, during the off-axis phase, the number of confined beam ions is ∼67% of the number in the on-axis phase. In that discharge, according to TRANSP, the beam energy transfered to the plasma in the off-axis phase (averaged over all four sources) is 85% of the transfered beam energy in the on-axis phase. In the off-axis (on-axis) phase, TRANSP computes that 22% (16%) of the injected energy is lost to shinethrough, 5% (3%) to prompt orbit loss to the walls and 11% (6%) to charge exchange. For the discharge of figure 9, the density is higher in the off-axis phase than the on-axis phase, so the computed shinethrough losses are only 25% in the off-axis phase compared with 28% in the on-axis phase. Because of the reduced shinethrough losses, even though the confinement degrades for off-axis injection, the predicted energy transferred to the plasma during the off-axis phase is 98% of the on-axis value. Experimentally, the inference from equation (1) is that the number of confined fast ions during the off-axis phase is ∼86% of the on-axis value.

In figure 9, the rise constant predicted by theory is normalized to give an average value close to experiment. Although an absolute measurement of the prompt confinement is desirable, the accuracy of the absolute neutron calibration and of knowledge of Z_{eff} (which determines n_d through quasineutrality) are too poor to permit a meaningful absolute comparison. (The normalization factor is consistent with the absolute calibration within the uncertainties.) On the other hand, for relative comparisons between sources, these uncertainties largely cancel, so the empirical comparison of the different injectors should be very accurate indeed. In the decay phase, the neutron decay rate depends on the electron temperature and density through the slowing-down time. These quantities are measured with sufficient accuracy to permit an absolute comparison with theory. Moreover, since uncertainties in the T_e and n_e profiles have a similar effect for all angles of beam injection, even small relative differences of a few per cent are meaningful.

A theoretical sensitivity study clearly illustrates the difference between absolute and relative accuracy (figure 10). In this study, the baseline case uses the solid profiles in figure 8, while each of the other cases replaces one of the profiles with a dashed profile. TRANSP analysis is performed, then the predicted neutron signals are fit to the rise and fall equations.

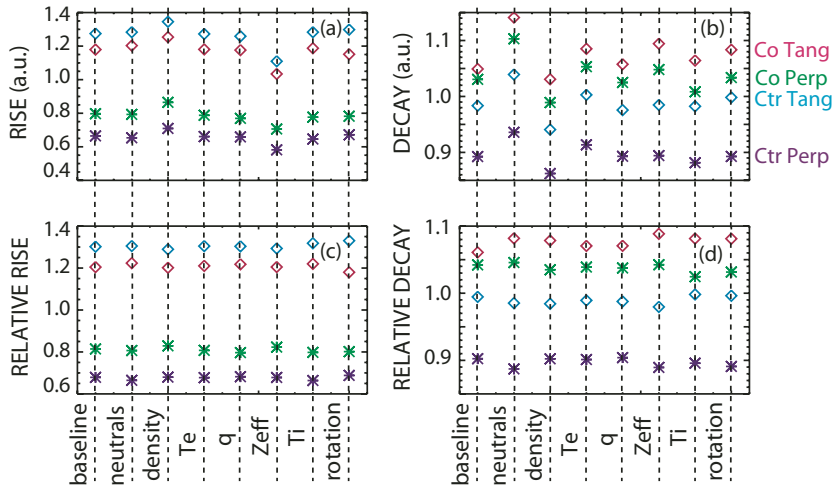

Figure 10. Fitted TRANSP (*a*) rate of rise and (*b*) decay time for the four different injection geometries. The results of eight different calculations are shown. The baseline case uses the solid-line profiles of figure 8. For each of the other calculations, one dashed-line profile from figure 8 is employed. In the lower figures, the rate of rise (*c*) and decay time (*d*) are normalized by the average value for the four injection angles.

The calculated rise changes ∼20% for plausible variations in n_e and Z_{eff} (figure 10(*a*)). The decay rate varies about 10% for plausible variations in plasma parameters, with the greatest sensitivities being to n_e and to the neutral density profile (figure 10(*b*)). On the other hand, if the rise and decay values are normalized to the average values of all four sources, the relative values only change a few per cent (figures 10(*c*) and (*d*)). It should be noted that this study is performed for an off-axis case where the uncertainties in profiles are relatively large, so the sensitivity is smaller for the on-axis discharges.

The absolute decay times are in reasonable agreement with the theoretical predictions for all of the discharges modeled by TRANSP for this study (figure 11). The degree of agreement with theory is comparable for all four injection angles and for both on-axis and off-axis injection. Overall, the ratio between experiment and theory is 98% with a correlation coefficient of $r = 0.94$. The observed differences are about twice as large as the estimated uncertainties.

The absolute decay measurements can also be compared with calculations that assume deviations from classical theory. Figure 12 compares the data with a set of TRANSP runs with increasing levels of postulated beam-ion diffusion D_B. For this case, the measured decay times agree best with an assumed value of diffusion of $D_B = 0\,m^2\,s^{-1}$. Some differences between the classical $D_B = 0$ prediction are larger than the estimated ∼10% sensitivity to plasma parameters but most of the classical predictions are within the uncertainty. The reduced χ^2 for $D_B = 0.5\,m^2\,s^{-1}$ is comparable to the classical case (∼30% higher). In contrast, values of fast-ion diffusion $\gtrsim 1.0\,m^2\,s^{-1}$ are clearly inconsistent with the data. The beam-ion diffusion is $<0.5\,m^2\,s^{-1}$ in this low-power discharge.

The insensitivity of the relative measurements to uncertainties in plasma parameters permits meaningful comparisons of different discharges. A database of all 302 beam blips has been compiled, with the rise and decay values normalized to running averages of the various sources. Figure 13 compares two full-size on-axis discharges with quite different

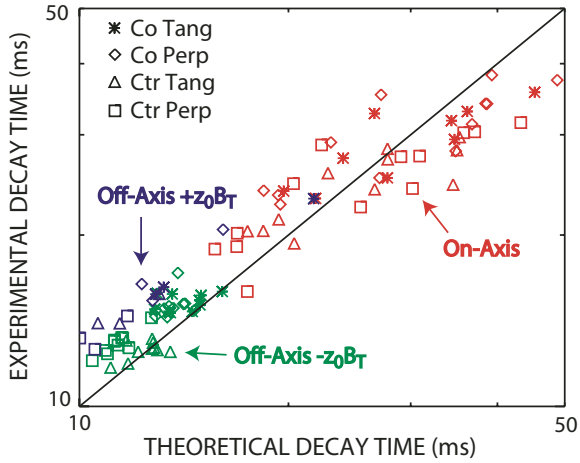

Figure 11. Experimental decay time versus decay time predicted by TRANSP for many different discharges. The angle of beam injection is represented by the symbols and the colors indicate on-axis injection, off-axis with $z_0 B_T > 0$ and $z_0 B_T < 0$. The solid line shows agreement between theory and experiment.

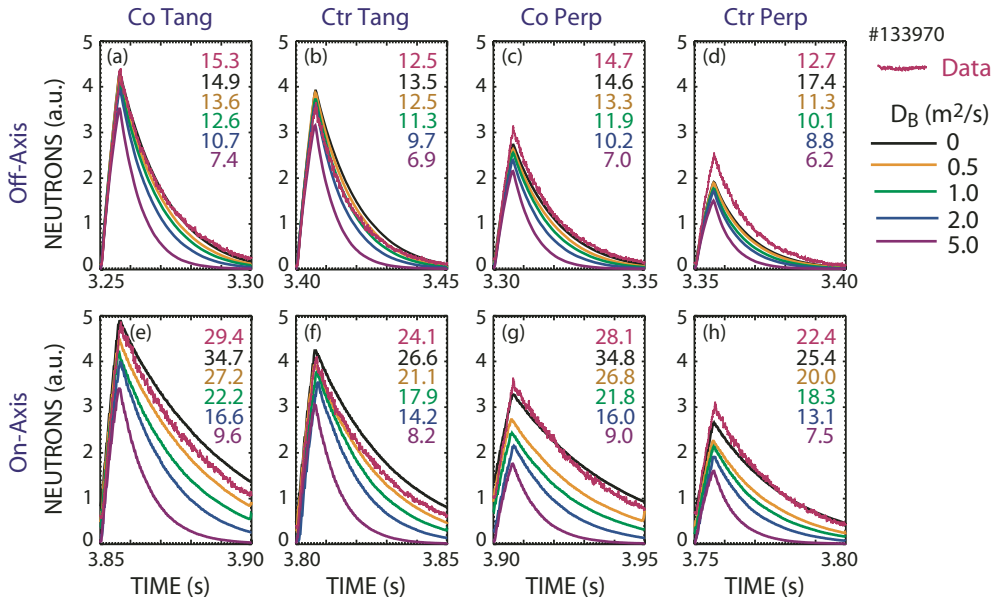

Figure 12. Measured neutron response (magenta) to a beam blip for injection into a small $B_T > 0$ plasma that was down-shifted (top row) then raised to the midplane (bottom row) for co-tangential (*a*), (*e*), counter-tangential (*b*), (*f*), co-perpendicular (*c*), (*g*) and counter-perpendicular (*d*), (*h*) injection. The TRANSP predictions for classical behavior ($D_B = 0$) and spatially uniform *ad hoc* beam-ion diffusion of 0.5, 1.0, 2.0 and 5.0 $m^2\ s^{-1}$ are also shown. The numbers in each panel show the fitted decay times for the various cases. $I_p = 0.9$ MA.

values of plasma current. As expected, the differences between injection angles are large at 0.6 MA when the poloidal gyroradius is large but become much smaller at 1.2 MA. The difference in prompt losses essentially vanishes at higher current but the difference in decay time between counter-injected beams and co-injected beams, though smaller, still persists.

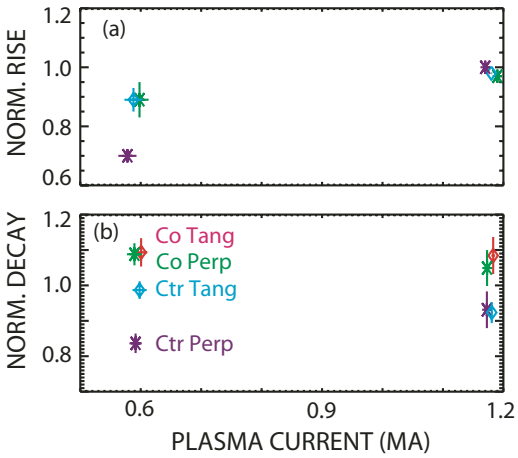

Figure 13. Normalized rate of rise (*a*) and decay rate (*b*) versus plasma current in a pair of full-size centered plasmas. The rise data are normalized to the co-tangential case, while the decay data are from the running average of the four beam types. The error bars represent the standard deviation of the data.

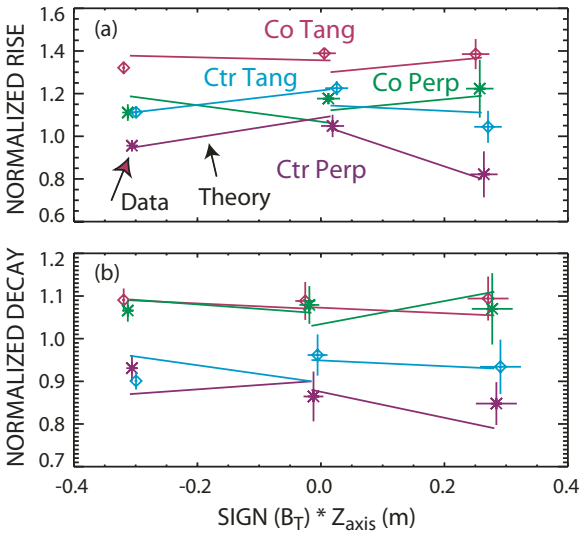

Figure 14. Average values of the normalized (*a*) rate of rise and (*b*) decay time versus $z_0 B_T/|B_T|$. Positive values of the abscissa correspond to a field helicity that is favorable for off-axis NBCD. The symbols represent the average and standard deviation of the blips in a database of 302 beam pulses. The solid lines represent the predicted theoretical variations for two cases that were analyzed by TRANSP. In all cases, the normalization is to the running average of the data or theory for all beam injection angles.

Another interesting quantity is the dependence on the field-line helicity (figure 14). For co-injection, there should be more passing particles at larger minor radius for positive sign of $z_0 B_T$ and vice versa for counter-injection. Experimentally, any difference in either the rise or the decay associated with the helicity is small. This is in contrast to the measured off-axis NBCD, which shows a strong dependence on helicity [37]. This weak dependence is probably

due to two countervailing trends: larger values of $|\chi|$ improve fast-ion confinement but larger average minor radius $\langle r \rangle$ degrades it. The theoretical predictions shown in figure 14 for some representative cases also show only a weak variation and the differences with experiment are comparable to the estimated uncertainties.

Analysis of the TRANSP output suggests the reasons for the empirical trends. As suggested by the representative orbits (figure 3) and sample distribution functions (figurre 4), prompt losses of large banana orbits account for the smaller rise of the counter-perpendicular beam. At the opposite extreme, the rise of the co-tangential beams is largest because this source produces many well-confined passing orbits. The rise of the counter-tangential beam is similar to the rise of the co-perpendicular beam because it launches more passing particles, which favors confinement, but the orbit shift after deposition is outward, which favors losses.

In both theory and experiment, the signals from the counter beams decay faster than the co beams. This seems to be due to the larger average minor radius of the counter population, which increases charge-exchange losses and also decreases the effective slowing-down time. According to TRANSP, delayed losses caused by pitch-angle scattering onto a loss orbit are negligible.

4. Neutron and FIDA data in beam-heated discharges

Figure 15 shows the response of the neutron rate and a central FIDA signal to cyclic injection of the four beam types for both on-axis and off-axis injection. The signals repetitively rise and fall with the different beam types. Since the 80 ms duration of injection of a particular beam type is comparable to the slowing-down time ($\tau_s \simeq 75$ ms), the signals evolve throughout each beam pulse.

Note that the time evolution of the neutron and FIDA signals differ. The fast-ion distribution function has a complicated dependence on phase space variables such as energy, pitch and position. The neutron and FIDA signals respond differently to the different sources because the two fast-ion diagnostics weight different regions in velocity space differently. The notion of a diagnostic 'weight' or 'instrument' function in phase space is extensively discussed in appendix A of [53], so only a brief summary is given here. The neutron diagnostic weights high-energy ions most heavily; ions with velocities that oppose the toroidal rotation are also favored. Above a certain low-energy cutoff, the vertical FIDA diagnostic samples most of velocity space but favors co-rotating ions. The FIDA imaging diagnostic accepts light from essentially all fast-ion energies but strongly favors ions with large counter velocities. (See figure 14 of [45] for a graphical representation of these weight functions.) The observed time evolution in figure 15 is consistent with these theoretical expectations. The neutron rate is largest during counter-tangential injection but the FIDA signal is largest during co-injection, as expected. Figure 16 of [45] shows a similar comparison that includes the FIDA imaging signal, which exhibits a very strong dependence on the counter-passing population.

Figure 15 also shows the predicted evolution of the neutron rate in this discharge. The agreement with experiment is good in the on-axis phase. In the off-axis phase, the predicted value is lower than experiment during co-tangential injection and higher than experiment during counter-tangential injection. According to TRANSP, the neutron signal in this discharge is produced almost entirely by high-energy beam ions, with 88% contributed by beam-plasma reactions, 10% by beam-beam reactions and 2% by thermonuclear reactions.

The theoretical prediction is sensitive to uncertainties in the plasma profiles that are input to the calculation. Plausible variations in the profiles (figure 8) result in $\sim$10% variations in the predicted neutron rate (figure 16(*a*)). As for the beam blip data, the sensitivity to profile errors is considerably smaller ($\lesssim$5%) when relative differences between sources are

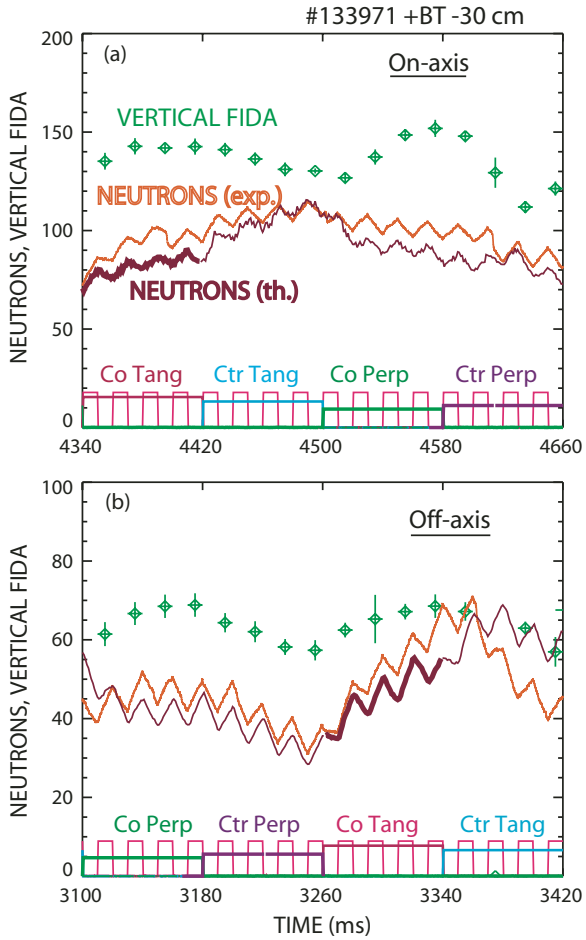

Figure 15. Time evolution of the neutron rate and of the $R = 180$ cm vertical FIDA channel during the (*a*) on-axis and (*b*) off-axis phase of an H-mode discharge. The 330L co-tangential beam viewed by the vertical FIDA diagnostic injects continuously at 50% duty cycle, while the steady source cycles through the four different angles of injection. The neutron rate predicted by TRANSP is most reliable during the phase marked by the thick line because toroidal rotation data is available then; the absolute calibration is adjusted 20% to facilitate comparison of the time evolution. The FIDA data are conditionally averaged over several cycles of beam injection. $I_p = 0.9$ MA; $B_T = +2.1$ T; $z_0 = -30$ cm during the off-axis phase; off-axis profiles shown in figure 8.

considered (figure 16(*c*)). There is one exception to this, however. The full CER profiles of toroidal rotation are only available when the co-tangential source at 30L is injected. Because the different sources alter the magnitude and direction of the torque input to the plasma, the evolution of the rotation profile is highly uncertain as the discharge cycles through the various sources. The more reliable theoretical predictions are indicated by the thick solid line in figure 15, while the periods indicated by the thin solid line have larger uncertainties of ∼10%.

Figure 16 also shows how the predicted neutron rate changes for various levels of spatially uniform *ad hoc* beam-ion diffusion in the TRANSP calculation. The predicted rate decreases rapidly with increasing D_B for all sources (figure 16(*b*)) but the relative difference between sources is barely affected (figure 16(*d*)).

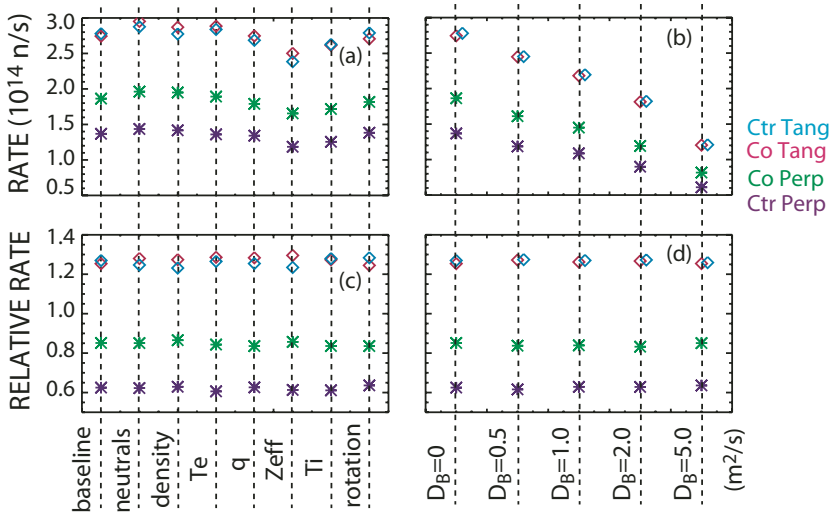

Figure 16. TRANSP predicted neutron rates for the four different injection geometries. The results of 12 different calculations are shown. The baseline case uses the solid-line profiles of figure 8. For each of the other calculations, either (*a*), (*c*) one dashed-line profile from figure 8 or (*b*), (*d*) the indicated spatially uniform *ad hoc* diffusion coefficient D_B (in $m^2\ s^{-1}$) is employed. In the lower figures, the neutron rate is normalized by the average value for the four injection angles.

Table 1. Measured and predicted relative neutron rates for the different angles of injection. An L-mode (H-mode) is indicated by 'L' ('H') and the sign of $z_0 B_T$ by a + or −. The italicized theoretical predictions have larger uncertainties because the toroidal rotation is unavailable during this phase of the discharge.

Shot	Condition	Co-tang. Exp (Theory)	Co-perp. Exp (Theory)	Ctr-tang. Exp (Theory)	Ctr-Perp. Exp (Theory)
132220	Full-size, L	1.07 ± 0.02 (0.99)		0.92 ± 0.01 (1.01)	
132607	On-axis H	0.98 ± 0.02 (0.99)		1.01 ± 0.02 (1.01)	
132607	Off (+) H	1.16 ± 0.03 (1.05)		0.82 ± 0.01 (0.94)	
133969	On-axis H	1.06 ± 0.02	1.01 ± 0.02	1.12 ± 0.10	0.84 ± 0.02
133969	Off (−) L	1.29 ± 0.03 (1.15)	0.94 ± 0.02 *(0.90)*	0.97 ± 0.02 *(1.25)*	0.75 ± 0.04 (0.71)
133969	Off (−) H	1.37 ± 0.01	1.04 ± 0.08	0.87 ± 0.02	0.76 ± 0.02
133971	On-axis H	1.04 ± 0.04 (1.03)	0.98 ± 0.01 *(0.92)*	1.13 ± 0.02 *(1.25)*	0.81 ± 0.02 (0.82)
133971	Off (−) H	1.31 ± 0.10 (1.16)	0.89 ± 0.12 *(0.95)*	0.93 ± 0.03 *(1.22)*	0.74 ± 0.01 (0.73)

The measured and predicted rates at the end of injection by a particular beam type for discharges with beam injection patterns like those shown in figures 6(*b*) and (*c*) are recorded in table 1. To minimize the sensitivity to uncertainties in plasma parameters and in the absolute calibration of the neutron detectors, the rates are normalized to the average rate for all of the sources utilized in that particular case. The experimental mean and standard deviation are obtained from multiple observations during the repetitive cycling of the various sources. As for the beam blip data, the counter-perpendicular source invariably produces the fewest neutrons for both on- and off-axis injection. Also, the co-tangential source is generally better than or comparable to the other sources. The agreement with theory is only fair. In agreement with experiment, theory always predicts that the counter-perpendicular beam will produce the lowest rate and the predicted value is in good quantitative agreement with the measured values. On the other hand, for the other sources, some of the predictions are consistent with

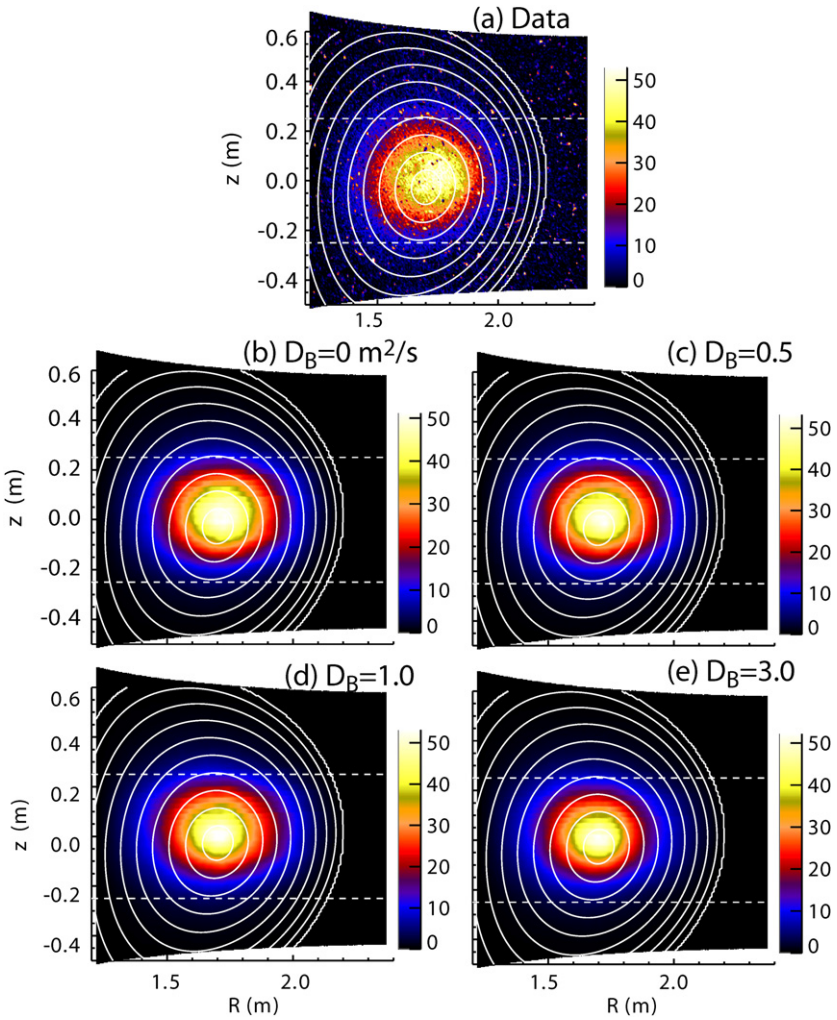

Figure 17. Measured (*a*) and predicted FIDA images for simulations with (*b*) classical, (*c*) $D_B = 0.5$, (*d*) $D_B = 1.0$ and (*e*) $D_B = 3.0\,m^2\,s^{-1}$ beam-ion diffusion during the on-axis phase of discharge #132607. The data are conditionally averaged during steady-state conditions; the time is just after the counter-tangential injection ends. $B_T = -2.1$ T; $I_p = 0.9$ MA; $\bar{n}_e = 2.7 \times 10^{19}\,m^{-3}$; $T_i(0) \simeq 6.5$ keV; $T_e(0) \simeq 4.5$ keV; H-mode.

the experimental values but some of the predictions differ by more than the ∼5% relative variations found in the sensitivity study (figure 16(*c*)).

High quality two-dimensional images of the FIDA light are available for one discharge. Some of these data were already published [37, 45]. The image is in quantitative agreement with the classical prediction for the on-axis case; the time evolution of the signal also agrees well with the prediction [45]. The off-axis profile is qualitatively consistent with a hollow fast-ion profile [37]. Here, these data are further analyzed in order to determine their implications for fast-ion transport. The selected analysis time is at the beginning of injection by the 30L imaging beam, just after the counter beam turns off (figure 6(*c*)). Figures 17 and 18 compare conditionally averaged images with simulated images for four different values of

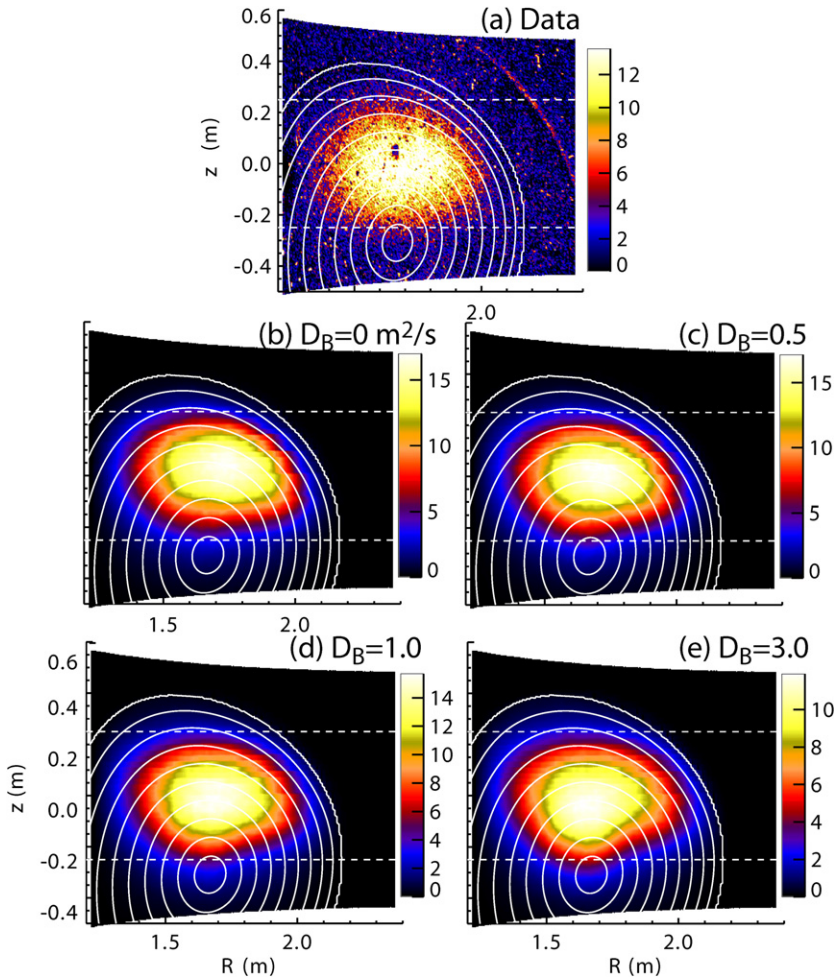

Figure 18. Same as figure 17 but during the off-axis ($z_0 = -30$ cm) phase. There is a low amplitude $n = 1$ tearing mode during this phase. $T_i(0) \simeq 3.6$ keV; $T_e(0) \simeq 2.2$ keV; H-mode.

ad hoc diffusion. The measured images are in good qualitative agreement with the predicted images. For spatially uniform diffusion, the simulated profiles are essentially isomorphic, with only the amplitude of the signal decreasing with increasing values of D_B. In order to determine the magnitude of the transport from these comparisons, it is necessary to know the absolute magnitude of the measured image but, unfortunately, for the 2008 data, the uncertainties in the filter-angle and intensity calibrations are too great to provide an accurate calibration. Quantitative analysis confirms that the data are consistent with theory (figure 19). In figure 19, the normalization between the data and the simulations is adjusted by an 'intensity scale factor' and the reduced chi-squared $\tilde{\chi}^2$ is computed for the four simulations as a function of this normalization factor. The results show that, with the proper choice of absolute calibration, essentially any value of spatially uniform D_B gives satisfactory agreement with experiment (minimum $\tilde{\chi}^2 \lesssim 1$). For the on-axis case, the agreement is best for $D_B = 0$–$1.0\,\mathrm{m}^2\,\mathrm{s}^{-1}$. The off-axis comparison is insensitive to the selected value of D_B. There is a constraint on the scale factor, however: the intensity calibration must be the same in both phases of the discharge. Inspection of figure 19 shows that, for modest values of D_B, the normalization that minimizes

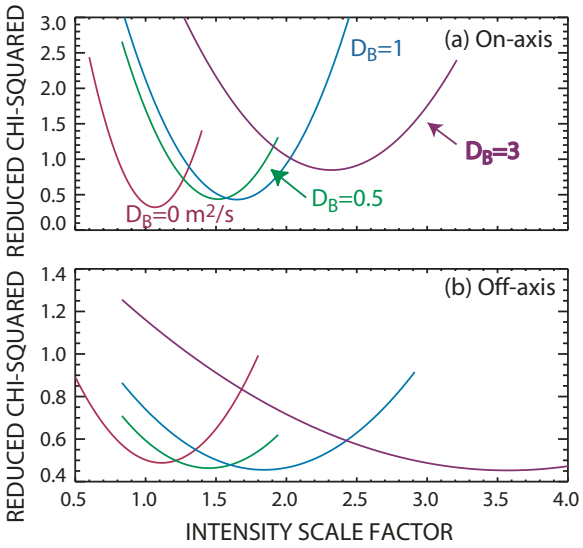

Figure 19. Reduced chi-squared $\tilde{\chi}_r^2$ versus intensity normalization factor for the data and simulations in (*a*) figure 17 and (*b*) figure 18.

$\tilde{\chi}^2$ during the on-axis phase also minimizes $\tilde{\chi}^2$ in the off-axis phase. This implies that the transport in the two phases of the discharge is similar.

Absolutely calibrated data are available for the vertical FIDA diagnostic. A typical set of spectra in a low-temperature L-mode discharge is shown in figure 20; these particular spectra are from the last 10 ms of injection by the co-tangential source during off-axis injection. The D_α transition is at 656.1 nm, so these data are from the blue-shifted wing of the spectrum, with higher velocities at smaller wavelength and lower velocities at longer wavelength. It is convenient to relate the Doppler-shifted wavelength to the energy E_λ of a neutral that has all of its velocity directed toward the collection lens. As discussed in [17], most of the light produced by full-energy ions from the co-tangential beams is in the wavelength range $E_\lambda = 30$–60 keV. The shape of the spectra in figure 20 is similar to the spectra published previously for MHD-quiescent plasmas [17]. Figure 20 also shows the spectral shape predicted by the FIDA simulation code for classical fast-ion behavior. The predicted spectral shape agrees well with experiment for the inner channels but deviates for the outermost channels, especially at lower Doppler shift. Figure 20(*h*) provides a quantitative comparison of the measured and simulated spectra. At large Doppler shift ($E_\lambda = 40$–60 keV), the reduced chi-squared $\tilde{\chi}^2$ is $\lesssim 1$, indicating satisfactory quantitative agreement between experiment and theory. At smaller Doppler shift ($E_\lambda = 20$–40 keV), $\tilde{\chi}^2$ exceeds unity, suggesting that the classical NUBEAM simulation may not include all of the relevant physics. Integration of the spectra over $E_\lambda = 30$–60 keV yields the spatial profile shown in figure 20(*i*). Given that this is an absolute comparison with no free parameters, the agreement seems reasonable, although the differences between experiment and theory do exceed the estimated random errors.

There are four likely sources of systematic error in this comparison, two for experiment and two for theory. The spectrometer is absolutely calibrated by placing a light source in the vessel but optical components darken during a campaign, introducing a likely uncertainty of $\sim$10%. A second source of experimental systematic error is in the background subtraction. One of the challenges in a FIDA measurement is to avoid scattered light associated with the very bright cold D_α line [36]. Recall that the FIDA signal is obtained by subtracting the background

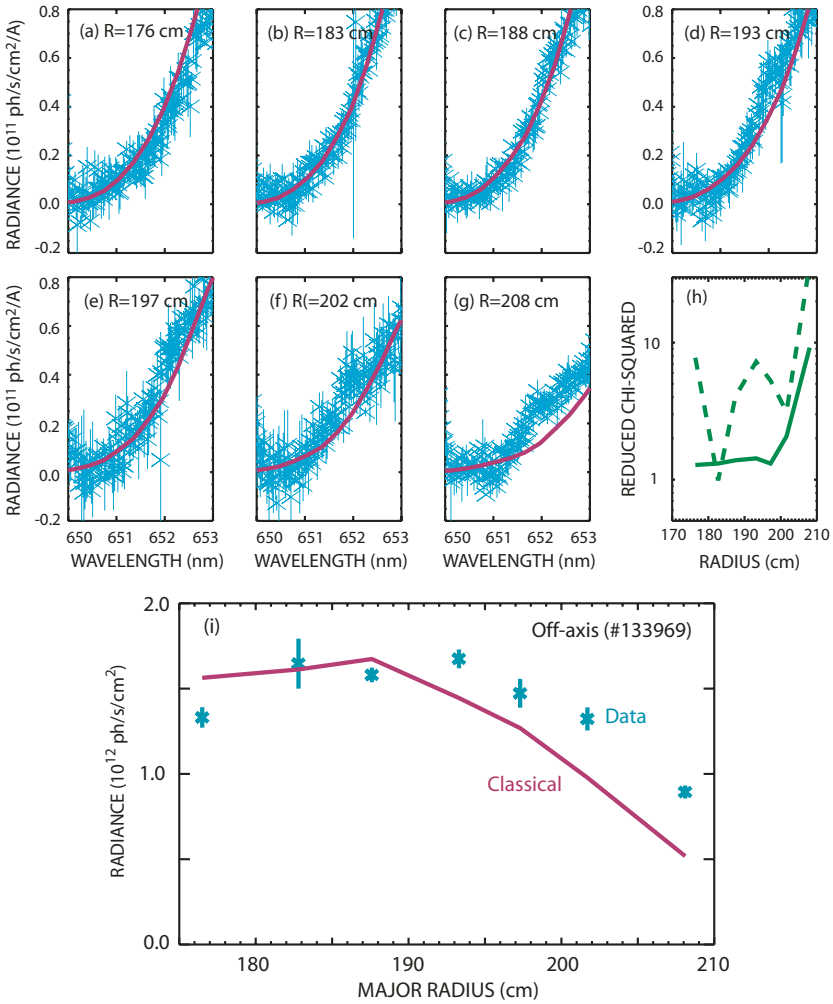

Figure 20. (*a*)–(*g*) FIDA spectra for the seven vertically viewing absolutely calibrated channels (symbols with error bars) and spectra predicted by the FIDA simulation code for classical fast-ion behavior (solid lines) near the end of injection by the co-tangential beam. The data are conditionally averaged over the steady-state portion of the off-axis phase of the discharge; the error bars are the uncertainty associated with background subtraction. (*h*) Reduced chi-squared $\tilde{\chi}_r^2$ of the spectra from each channel for $E_\lambda = 40$–60 keV (solid line) and for $E_\lambda = 20$–40 keV (dashed). (*i*) Spatial profile after integration of the spectra between $E_\lambda = 30$–60 keV. $B_T = +2.1$ T; $z_0 = -30$ cm; $I_p = 0.9$ MA; $T_i(0) \simeq 1.6$ keV; $T_e(0) \simeq 1.9$ keV; L-mode.

light obtained when the 330L imaging beam is off from the total light when the 330L beam is on. In L-mode, the edge background light is nearly constant (figure 21(*b*)); the results are highly reproducible for every beam pulse of the same type and, with conditional averaging, the random error associated with background subtraction essentially vanishes. However, background light that is *only* present when the active beam is on could still introduce a small systematic error. For example, beam-emission light from the 330L source could scatter within the spectrometer, elevating the background. In H-mode, both random and systematic errors in the background subtraction are larger. During ELMs, edge impurity light and scattered Dα light can change rapidly, so the background is no longer constant in time. With many repetitive

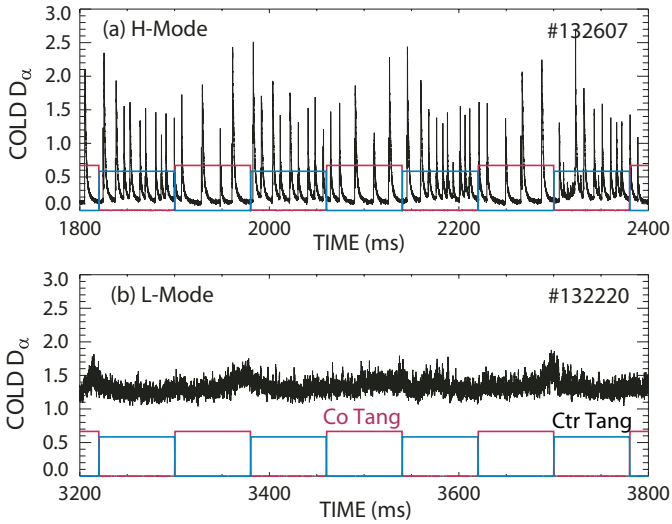

Figure 21. Time evolution of the cold D_α light in an (*a*) ELMy H-mode and a (*b*) L-mode discharge with repetitive cycling of the co-tangential and counter-tangential beams. (The 330L co-tangential beam used for vertical FIDA measurements injects continously at 50% duty cycle in both discharges.) (*a*) $B_T = -2.1$ T; $z_0 = -30$ cm; $I_p = 0.9$ MA. (*b*) Full-size on-axis shape; $B_T = 2.0$ T; $I_p = 0.6$ MA.

pulses, acceptable background subtraction can still be achieved but only if the ELM behavior is stationary. As shown in figure 21(*a*), this is not always the case in these discharges. Under some conditions, the ELM frequency has a clear cyclic dependence on beam angle. Although the random errors associated with background subtraction are acceptable, in these cases, there could be a systematic error when comparing FIDA measurements for different sources.

There are also two likely sources of error in the simulated FIDA signals. One source of error is in the atomic physics. The intensity of the FIDA light is proportional to the fraction of neutrals that occupy the $n = 3$ energy level. For excited n levels, the excitation and charge-exchange cross sections have ∼20% uncertainties, which may introduce an error in the predicted intensity of 10–20%. Another source of error is the uncertainties in the plasma profiles that are input to the calculation. A sensitivity study using the profiles in figure 8 shows that the simulated spectra and profiles are not terribly sensitive to the uncertainties in plasma parameters (figure 22). The strongest dependence in the spectral shape is on the background neutral density profile at low Doppler shift and large major radius. This is the expected effect of charge-exchange losses: in solutions of the Fokker–Planck equation with $\nu_{cx} \sim \nu_E$, the distribution function is most distorted at low velocities (see, e.g. [54]). (ν_{cx} is the charge-exchange loss rate.) For off-axis injection, the variations in the spatial profile associated with uncertainties in the plasma parameters are at the ∼20% level. (The uncertainties are 10–15% for on-axis injection.)

To summarize, the discrepancies between classical theory and the data shown in figure 20 might be attributed to systematic error but larger differences are meaningful, particularly when comparing discharges acquired on the same day.

Deviations that are larger than the estimated uncertainties are often observed. Figure 23 shows the spectra from an H-mode discharge acquired on the same day as the discharge in figure 20; the same co-tangential source was injected in both plasmas. Near the magnetic axis, the spectral shape resembles the prediction but the intensity is significantly less than classically predicted. At larger major radii, the spectral shape differs markedly from the

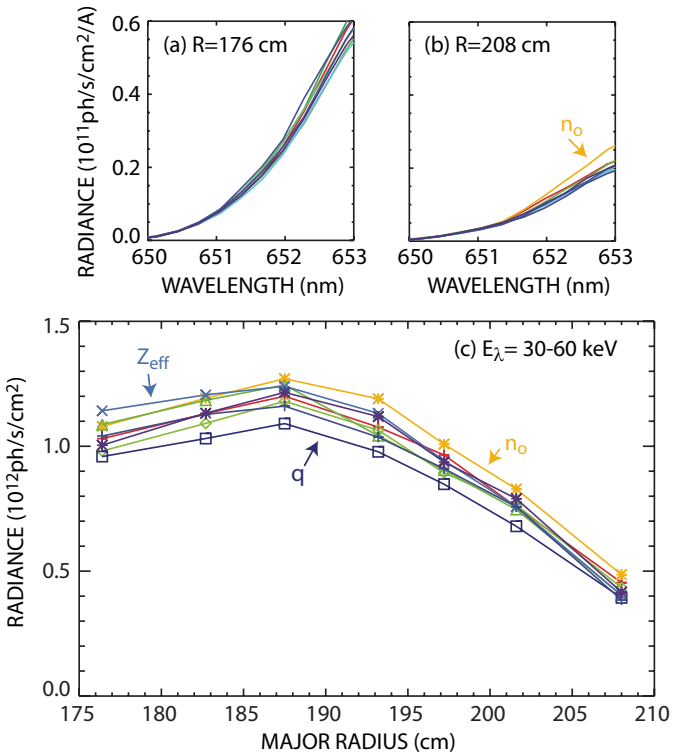

Figure 22. Sensitivity of the predicted FIDA spectra for the channels at (*a*) $R = 176$ cm and (*b*) $R = 208$ cm and of (*c*) the FIDA profile after integration over $E_\lambda = 30$–60 keV for the eight different cases indicated in figure 8.

theoretical prediction. Quantitatively, $\tilde{\chi}^2$ is significantly larger than one for nearly all radii and wavelength bands, indicating that the classical NUBEAM distribution function does not describe the experiment.

Deviations between theory and experiment are observed for all four angles of injection. As for the neutrons, the general trends are consistent with the NUBEAM predictions but the discrepancies are larger than the estimated uncertainties. For example, in the discharge of figure 24, the counter perpendicular beam produces the least light but the radial profile shape differs markedly from the prediction. Also, although the co-perpendicular beam produces a relatively bright FIDA signal, its magnitude is significantly smaller than predicted. Figure 25 shows an example from a full-size, 0.6 MA, sawtoothing, L-mode plasma with co- and counter-tangential injection but no perpendicular injection. The difference between co- and counter-injection is correctly predicted but the magnitude of the signal is smaller than expected at nearly all radii. The data agree better with simulations that include *ad hoc* diffusion of $D_B \simeq 1.0\,m^2\,s^{-1}$ than with the classical prediction. Deviations are observed both inside and outside of the sawtooth inversion radius.

The dependence of the distribution function on the helicity of the magnetic field shows the expected qualitative trend. Figure 26 shows central FIDA spectra and the neutron rate for two nearly identical discharges with opposite values of magnetic pitch during steady off-axis co-tangential injection (figure 6(*d*)). As expected, the FIDA light and neutron rate are both larger for $z_0 B_T < 0$ than for $z_0 B_T > 0$. On the other hand, the simulations are in poor

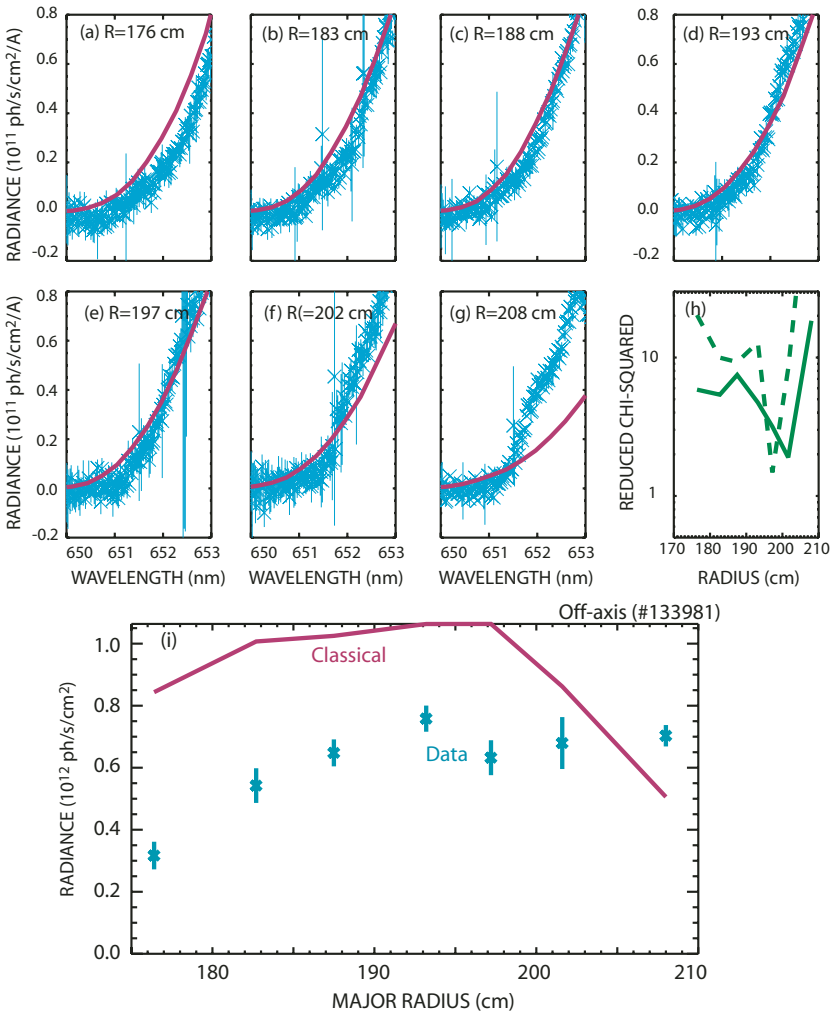

Figure 23. (*a*)–(*g*) FIDA spectra for the 7 vertically viewing absolutely calibrated channels (symbols with error bars) and spectra predicted by the FIDA simulation code for classical fast-ion behavior (solid lines) during steady injection by the co-tangential beam. The error bars are the uncertainty associated with background subtraction. (*h*) Reduced chi-squared $\tilde{\chi}_r^2$ of the spectra from each channel for $E_\lambda = 40$–60 keV (solid line) and for $E_\lambda = 20$–40 keV (dashed). (*i*) Spatial profile after integration of the spectra between $E_\lambda = 30$–60 keV. $B_T = +2.1$ T; $z_0 = -30$ cm; $I_p = 0.9$ MA; $T_i(0) \simeq 3.4$ keV; $T_e(0) \simeq 2.3$ keV; H-mode.

quantitative agreement with the data. In particular, the spectral shape, FIDA profile and magnitude of the change in neutron rate are larger than the estimated uncertainties in the theoretical predictions.

5. Interpretation: microturbulence causes the discrepancies

It is well known that sawteeth, tearing modes and Alfvén modes can cause fast-ion transport. In this section, we focus on discrepancies with classical theory that are not associated with fast-ion instabilities or MHD. For the anomalous cases shown in the previous section, the spectral

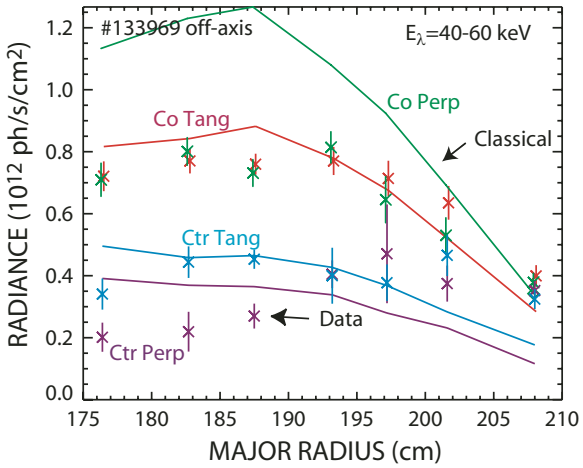

Figure 24. Vertical FIDA profiles (symbols) in the last 10 ms of injection by each of the beam types and predicted profiles (lines) for classical behavior. Spectra integrated over $E_\lambda = 40$–60 keV. Same discharge as figure 20.

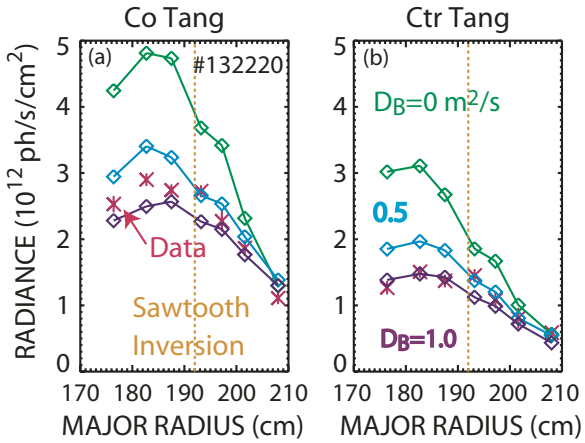

Figure 25. Vertical FIDA profile (x) near the end of co-tangential (a) and counter-tangential (b) injection in a full-size, on-axis, discharge. After conditional averaging, the random errors are smaller than the symbols in this steady-state L-mode discharge. The solid lines are the predicted profiles for *ad hoc* diffusion of $D_B = 0$, 0.5 and 1.0 $m^2\,s^{-1}$. The vertical dashed line indicates the sawtooth inversion radius inferred from ECE data. $B_T = -2.0$ T; $I_p = 0.6$ MA; $\bar{n}_e = 1.9 \times 10^{19}\ m^{-3}$; $T_i(0) = 2.9$ keV; $T_e(0) = 3.4$ keV.

shape deviates from the classical prediction, the shape is a function of radius and the radial profile differs markedly from the theoretical prediction (figures 23 and 24). Three properties are noteworthy.

1. The discrepancy between theory and experiment is often smaller at large Dopper shift than at small Doppler shift.
2. At small minor radius, the large Doppler shift portion of the spectrum is depleted relative to theory. At larger minor radius, the small Doppler shift portion of the spectrum is often larger than predicted.
3. When anomalies occur, they usually occur for all injection angles.

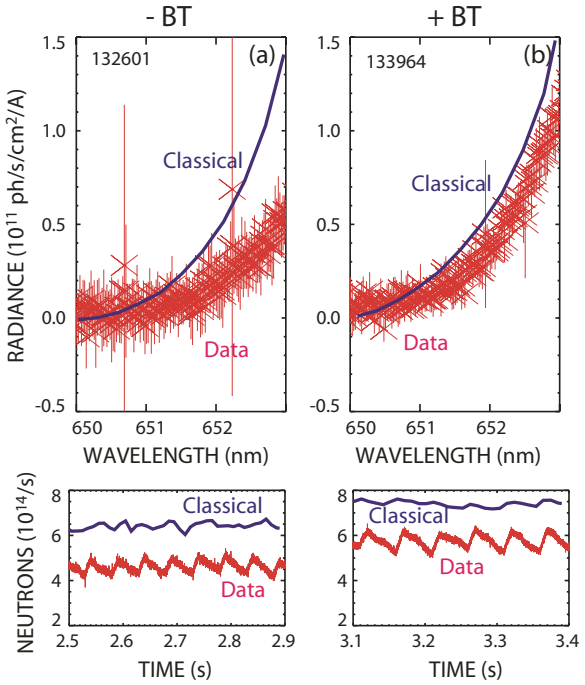

Figure 26. Comparison of two similar discharges with opposite field helicities: $z_0 B_T > 0$ (*a*), (*c*) and $z_0 B_T < 0$ (*b*), (*d*). (*a*), (*b*) FIDA data (symbols) and classical prediction (solid lines) for the $R = 176$ cm channel. (*c*), (*d*) Measured (red) and predicted (blue) neutron rates. $B_T = \pm 2.1$ T; $z_0 = -30$ cm; $I_p = 0.9$ MA; $\bar{n}_e = 3.5 \times 10^{19}$ m^{-3}. $T_i(0) \simeq 4.0$ keV; $T_e(0) \simeq 3.0$ keV.

These properties are consistent with theories that predict that fast-ion transport by microturbulence depends on the efficacy of phase-averaging. Large Doppler shifts are less altered than smaller Doppler shifts (property #1) because the energetic ions that produce large shifts have larger values of E/T. The second property is also expected. Near the magnetic axis, the plasma temperature is higher, so E/T is smaller and full-energy ions that produce large Doppler shifts suffer transport. At larger minor radius, the low Doppler shift portion of the signal is enhanced by fast ions that diffuse from the center. The third property is expected because all pitch angles are affected by microturbulence. For example, in the theory of [30], the diffusivity decreases as $E^{-1.5}$ for passing particles and as E^{-2} for trapped particles. Since this dependence is relatively weak and since the FIDA diagnostic effectively averages over much of velocity space, little dependence on injection angle is expected for transport by microturbulence.

If microturbulence is responsible for the anomalies, at the same radius, the discrepancies should be more pronounced at higher temperature (smaller E/T). Figure 27 shows the ratio of the experimentally measured radiance to classically-predicted radiance as a function of ion temperature for all of the cases analyzed in this study. If the effect of turbulent transport becomes increasingly important at low values of E/T, the anomaly should increase with increasing temperature (for fixed injection energy, as is the case here). The data follow the expected trend with a correlation coefficient of $r = -0.67$. (The correlation with central electron temperature is similar: $r = -0.58$.) Some of the scatter in the fit may be caused by different microturbulence properties in different discharges; for example, the L-mode case with $T_i \simeq 3.0$ exhibits a larger anomaly than otherwise similar H-mode discharges.

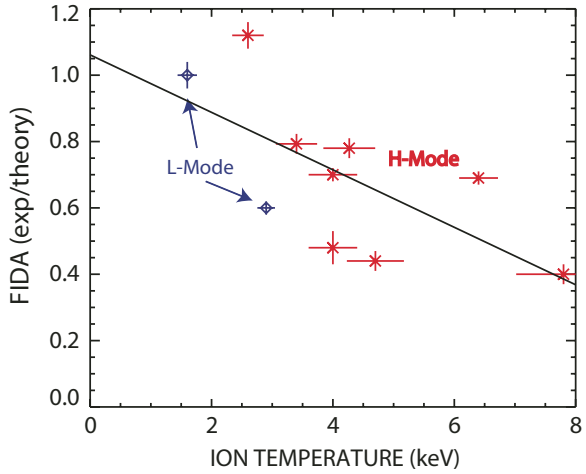

Figure 27. Ratio of the measured to classically predicted radiance for the $R = 183$ cm vertical FIDA channel versus central ion temperature for all of the analyzed cases with co-tangential injection. $E_\lambda = 20$–68 keV.

A power scan of four NBCD discharges (figures 6(*d*) and 7) confirms this trend. In these discharges, the ion and electron temperatures both increase monotonically as the beam power is increased from 3.1 to 7.2 MW. At low temperature, many of the vertical FIDA channels are consistent with classical theory but, as the power increases, the discrepancy increases and less light is observed than theoretically predicted (figure 28(*c*)). The neutron rate exhibits a similar dependence but the degradation with increasing temperature is more gradual (figure 28(*a*)). (For this comparison, the calibration of the neutron signal has been adjusted to make the ratio of experiment-to-theory approximately unity at low beam power.) The weaker dependence of the neutron rate is expected for two reasons: the neutron signal is volume-averaged, which reduces the sensitivity to spatial transport, and the neutron signal is more sensitive to higher energy ions than the FIDA signal, which weights the measurement toward higher values of E/T. Reconstructions of the equilibria using MSE data provide additional information about the beam-driven current and fast-ion pressure profile p_f [37]. The degradation in beam-driven current and p_f with beam power is similar to the neutron degradation (figure 28(*a*)). Since beam-driven current scales with $v_\parallel$ and is volume-averaged, this measurement, like the neutrons, should be less sensitive to temperature than the FIDA data. Similarly, the v^2 weighting of the fast-ion pressure measurement also makes p_f less sensitive to temperature effects than FIDA. It should be noted that the two highest power discharges in this sequence have a weak intermittent tearing mode and hints of Alfvén activity, respectively, but the relatively small levels are unlikely to cause appreciable fast-ion transport.

The magnitude of the discrepancies are consistent with the hypothesis that microturbulence causes 'anomalous' diffusion. A series of NUBEAM simulations using diffusion coefficients D_B loosely based on theory are performed. Theoretically [30], the fast-ion diffusion coefficient is

$$D_B \simeq c(E/T(r))D_i(r), \tag{2}$$

where $D_i(r)$ is the thermal-ion diffusivity and $c(E/T(r))$ is a function that describes the efficacy of phase-averaging. Here, we obtain $c(E/T)$ from figure 3 of [30] for a representative pitch angle of $\chi = 0.7$ and approximate $D_i(r)$ by the ion heat diffusivity $\chi_i(r)$ computed by

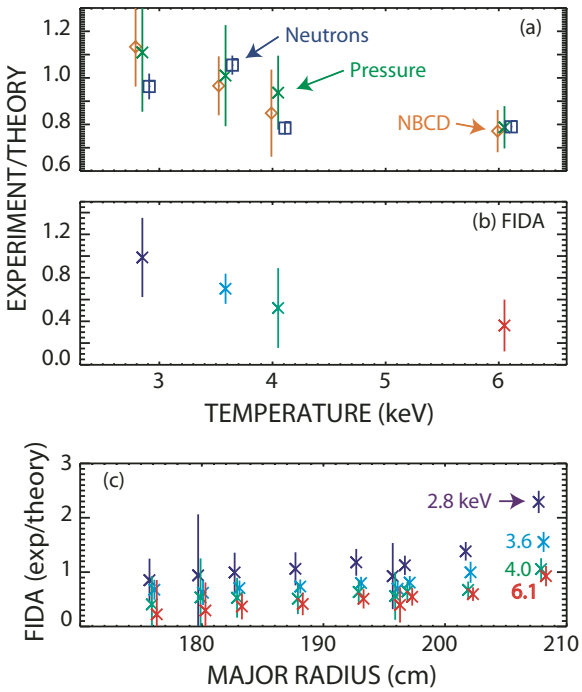

Figure 28. (*a*) Ratio of measured to predicted neutron rate (square), beam-driven current (diamond) and fast-ion pressure p_f at $\rho = 0.6$ (x) and (b) vertical FIDA radiance for the $R = 183$ cm channel as a function of the average of the central electron and ion temperature, $(T_e + T_i)/2$. (c) Ratio of measured to predicted vertical FIDA radiance versus major radius for the same four discharges. $E_\lambda = 20$–68 keV; $B_T = +2.1$ T; $z_0 = +23$ cm; $I_p = 0.9$ MA; $\bar{n}_e = 3.0$–3.4×10^{19} m^{-3}; co-tangential injection. The neutron error bars are from counting statistics. The FIDA, NBCD, and p_f error bars represent random errors inferred from the variance of the time series during the stationary phase of the discharge.

TRANSP for the classical case. NUBEAM allows a spatially dependent, energy-dependent *ad hoc* diffusion coefficient but the model assumes that the energy and radial dependences are separable, i.e. $D_B = g(E)h(r)$. (Here, g and h are arbitrary functions.) The NUBEAM model cannot replicate equation (2) exactly. Also, the $\chi_i(r)$ profile inferred from power balance depends on D_B so, in principle, multiple simulations are required to obtain a consistent solution. Despite these difficulties, the available tools suffice for a quantitative estimate. Numerous simulations with various combinations of $g(E)h(r)$ designed to approximate equation (2) result in two conclusions.

1. The theory-based diffusion coefficient is approximately the correct magnitude to account for the neutron, NBCD and FIDA discrepancies. In particular, the variation of T_i in the power scan is in the proper range of E/T to cause appreciable reductions in predicted signal for the high power cases but small effects for the low-power discharge.
2. The available separable model for D_B cannot reproduce the measured FIDA spectra or radial profile. Figure 29 shows an example of one such comparison. (The results for more complicated combinations of $g(E)h(r)$ are similar.) The magnitude of the signal agrees better with experiment for the theory-based diffusion coefficient than for the classical prediction but the shape of the profile and the shape of the spectra (particularly at larger minor radius) are still inconsistent.

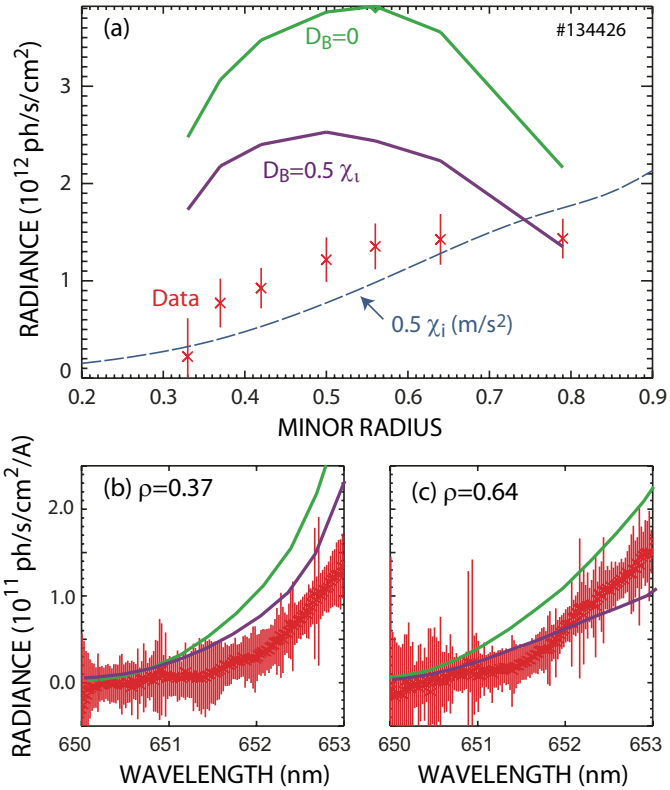

Figure 29. (*a*) FIDA radiance for $E_\lambda = 33$–60 keV versus normalized minor radius for the highest temperature discharge of figure 28. The data are indicated by symbols and the solid lines show the predicted profiles for the classical case and for a simulation that uses spatially variable *ad hoc* diffusion of $D_B = 0.5\chi_i$ (dashed line). Details of the spectral radiance for an inner and outer channel are shown in (*b*) and (*c*), respectively.

The assumption that ion-temperature gradient drift-wave turbulence exists in these discharges is consistent with the observed fluctuations. Because of the off-axis beam injection and unfavorable field-line pitch, the beam-emission spectroscopy (BES) diagnostic [55] has poorer spatial resolution than usual but the available data do show very-low wavenumber ($k_\perp \rho_i \ll 1$) broadband fluctuations in the 100–250 kHz range (figure 30). For the pair of H-mode plasmas shown in figure 30, the fluctuations are larger in the higher temperature discharge with the greater degradation in fast-ion confinement. The fluctuation amplitude tends to increase with radius and has a radial correlation length of a few centimeters.

6. Conclusions

The neutron and FIDA data lead to the following empirical conclusions about NBI into DIII-D.

- Co-tangential injection results in the best fast-ion confinement and counter-perpendicular injection results in the worst confinement (even when the confinement deviates from classical).
- The counter-injected beams disappear faster (through thermalization and/or charge-exchange losses) than the co-injected beams.

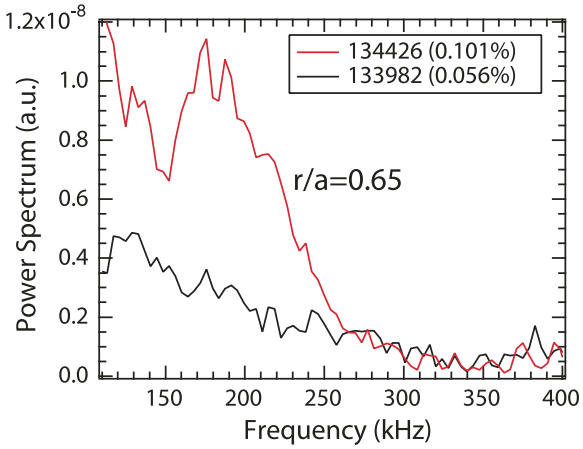

Figure 30. Power spectra measured by BES for the two highest temperature discharges shown in figure 28. The numbers in the legend are a relative measure of the fluctuation amplitude level.

- The difference between injection angles increases with increasing poloidal gyroradius.
- In contrast to off-axis NBCD, which shows a strong sensitivity to the field-line pitch, the fast-ion density does not depend strongly on field-line pitch.

Classical TRANSP simulations supply the following additional conclusions.

1. All of the empirical trends noted above are in qualitative agreement with the expected dependences. (This is primarily a test of the orbit topology as calculated by TRANSP.)
2. At low temperature, the spectral shape measured by FIDA is often consistent with the simulation. (This is primarily a test of the modeling of Coulomb scattering in TRANSP.)
3. The two-dimensional FIDA images are consistent with classical theory. (This tests beam deposition, orbital effects and Coulomb scattering.)
4. In many cases, the quantitative difference between the simulation and the measurement is larger than the estimated random and systematic uncertainties. In particular, the simulation predicts that counter-tangential beam blips produce larger neutron rates than co-perpendicular blips but the opposite is observed experimentally. During steady injection, the differences between sources often exceed the estimated uncertainties.
5. At low power, any anomalous fast-ion transport is small ($<0.5\,\mathrm{m^2\,s^{-1}}$). (The thermal-ion conductivity is $>1\,\mathrm{m^2\,s^{-1}}$.)
6. When anomalies in the FIDA profile occur, they usually occur for all injection angles.
7. The discrepancy between classical theory and experiment is usually smaller at large Doppler shift than at small Dopper shift.
8. The magnitude of the discrepancy between classical theory and experiment tends to increase with increasing temperature.

Apart from the neglect of turbulent transport, there are no obvious deficiencies in the TRANSP model. All of the confinement trends are in qualitative agreement with basic orbit theory: co-injection is better than counter-injection, near-tangential injection is better than near-perpendicular injection, on-axis injection is better than off-axis injection, high plasma current is better than low plasma current. Although the discrepancies are often larger than the estimated errors, there are no systematic discrepancies that appear throughout the entire data set that could be attributed to an error in the properties of a particular beam source, for

example. The deposition, orbit, Coulomb scattering and charge-exchange models employed in the NUBEAM module of TRANSP [38] adequately describe the fast-ion behavior in MHD-quiescent, low-temperature plasmas. However, for smaller values of fast-ion energy to temperature ($E/T \lesssim 10$), systematic discrepancies appear. The energy and temperature dependences of these discrepancies suggest that fast-ion transport by microturbulence is the culprit.

Quantitatively, the transport levels agree with a theory of fluctuation-induced transport that assumes the validity of phase-averaging. Although the accuracy of the experiment is inadequate to determine the precise scaling of the transport with fast-ion energy, the evident dependence of the discrepancies on temperature confirms that phase-averaging is operative.

In the future, we plan to reproduce the anomalies in plasmas with well-diagnosed microturbulence measurements and absolutely calibrated two-dimensional FIDA imaging. Once simulations that are consistent with the observed fluctuations are obtained, the expected fast-ion transport will be computed and compared with the fast-ion measurements.

Acknowledgments

The authors gratefully acknowledge the assistance of K Burrell, B Grierson, R Groebner, Deyong Liu, Yadong Luo, T Osborne, D Pace, R Prater, E Ruskov, Yubao Zhu and the entire DIII-D team. Wenlu Zhang kindly provided data from [30]. This work was supported by the US Department of Energy under SC-G903402 and DE-FC02-04ER54698.

References

[1] Wong K L *et al* 1991 *Phys. Rev. Lett.* **66** 1874
[2] Heidbrink W W, Strait E J, Doyle E, Sager G and Snider R T 1991 *Nucl. Fusion* **31** 1635
[3] Heidbrink W W and Sadler G J 1994 *Nucl. Fusion* **34** 535
[4] ITER Physics Expert Group on Energetic Particles, Heating, and Current Drive *et al* 1999 *Nucl. Fusion* **39** 2471
[5] Akers R J *et al* 2002 *Nucl. Fusion* **42** 122
[6] Bindslev H *et al* 2006 *Phys. Rev. Lett.* **97** 205005
[7] Bindslev H *et al* 2007 *Plasma Phys. Control. Fusion* **49** B551
[8] Degrassie J S, Groebner R J and Burrell K H 2006 *Phys. Plasmas* **13** 112507
[9] Hawkes N C *et al* 2005 *Plasma Phys. Control. Fusion* **47** 1475
[10] Heidbrink W W *et al* 2001 *Plasma Phys. Control. Fusion* **44** 373
[11] Heidbrink W W 2002 *Plasma Phys.* **9** 28
[12] Heidbrink W W *et al* 2003 *Nucl. Fusion* **43** 883
[13] Heidbrink W W, Burrell K H, Luo Y, Pablant N A and Ruskov E 2004 *Plasma Phys. Control. Fusion* **46** 1855
[14] Henriksson H *et al* 2005 *Plasma Phys. Control. Fusion* **47** 1763
[15] Hynoönen V *et al* 2007 *Plasma Phys. Control. Fusion* **49** 151
[16] Jarvis O N and Conroy S 2002 *Plasma Phys. Control. Fusion* **44** 1651
[17] Luo Y, Heidbrink W W, Ruskov E, Burrell K H and Solomon W M 2007 *Phys. Plasmas* **14** 112503
[18] Sato M *et al* 2002 *Nucl. Fusion* **42** 1008
[19] Stork D *et al* 2005 *Nucl. Fusion* **45** S181
[20] Tournianski M R, Akers R J, Carolan P G and Keeling D L 2005 *Plasma Phys. Control. Fusion* **47** 671
[21] Yoshida M *et al* 2006 *Plasma Phys. Control. Fusion* **48** 1673
[22] Naitou H, Kamimura T and Dawson J M 1979 *J. Phys. Soc. Japan* **46** 258
[23] Manfredi G and Dendy R O 1996 *Phys. Rev. Lett.* **76** 4360
[24] Manfredi G and Dendy R O 1997 *Phys. Plasmas* **4** 628
[25] Günter *et al* 2007 *Nucl. Fusion* **47** 920
[26] Suzuki T *et al* 2008 *Nucl. Fusion* **48** 045002
[27] Baranov Y F *et al* 2009 *Plasma Phys. Control. Fusion* **51** 044004
[28] Vlad M, Spineanu F, Itoh S, Yagi M and Itoh K 2005 *Plasma Phys. Control. Fusion* **47** 1015
[29] Hauff T and Jenko F 2007 *Phys. Plasmas* **14** 092301

[30] Zhang W, Lin Z and Chen L 2008 *Phys. Rev. Lett.* **101** 095001
[31] Hauff T, Pueschel M J, Dannert T and Jenko F 2009 *Phys. Rev. Lett.* **102** 075004
[32] Hauff T and Jenko F 2008 *Phys. Plasmas* **15** 112307
[33] Dannert T *et al* 2008 *Phys. Plasmas* **15** 062508
[34] Estrada-Mila C, Candy J and Waltz R E 2006 *Phys. Plasmas* **13** 112303
[35] Angioni C and Peeters A G 2008 *Phys. Plasmas* **15** 052307
[36] Luo Y, Heidbrink W W, Burrell K H, Kaplan D H and Gohil P 2007 *Rev. Sci. Instrum.* **78** 033505
[37] Park J M *et al* 2009 *Phys. Plasmas* **16** 092508
[38] Pankin A, Mccune D, Andre R, Bateman G and Kritz A 2004 *Comput. Phys. Commun.* **159** 157
[39] Heidbrink W W, Murakami M, Park J M, Petty C C and Van Zeeland M A 2009 *Phys. Rev. Lett.* **102** submitted
[40] Rice B W, Nilson D G and Wroblewski D 1995 *Rev. Sci. Instrum.* **66** 373
[41] Rome J A, Mcalees D G, Callen J D and Fowler R H 1976 *Nucl. Fusion* **16** 55
[42] Murakami M *et al* 2009 *Nucl. Fusion* **49** 065031
[43] Heidbrink W W, Taylor P L and Phillips J A 1997 *Rev. Sci. Instrum.* **68** 536
[44] Zankl G *et al* 1981 *Nucl. Instrum. Methods* **185** 321
[45] Van Zeeland M A, Heidbrink W W and Yu J 2009 *Plasma Phys. Control. Fusion* **51** 055001
[46] Porter G D 1998 *Phys. Plasmas* **5** 4311
[47] Carlstrom T N *et al* 1992 *Rev. Sci. Instrum.* **63** 4901
[48] Austin M E and Lohr J 2003 *Rev. Sci. Instrum.* **74** 1457
[49] Gohil P, Burrell K H, Groebner R J and Seraydarian R P 1990 *Rev. Sci. Instrum.* **61** 2949
[50] Strait E J 1996 *Rev. Sci. Instrum.* **67** 2538
[51] Van Zeeland M A *et al* 2006 *Phys. Rev. Lett.* **97** 135001
[52] Van Zeeland M A *et al* 2005 *Plasma Phys. Control. Fusion* **47** L31
[53] Heidbrink W W *et al* 2007 *Plasma Phys. Control. Fusion* **49** 1457
[54] Goldston R J 1975 *Nucl. Fusion* **15** 651
[55] Gupta D K, Fonck R J, Mckee G R, Schlossberg D J and Shafer M W 2004 *Rev. Sci. Instrum.* **75** 3493